The Astrophysical Journal, 948:24 (19pp), 2023 May 1 https://doi.org/10.3847/1538-4357/acc8c7


# Structure of the Plasma near the Heliospheric Current Sheet as Seen by WISPR/Parker Solar Probe from inside the Streamer Belt

Paulett C. Liewer[1], Angelos Vourlidas[2], Guillermo Stenborg[2], Russell A. Howard[2], Jiong Qiu[3], Paulo Penteado[1], Olga Panasenco[4], and Carlos R. Braga[5]
[1] Jet Propulsion Laboratory, California Institute of Technology, Pasadena, CA, 91109, USA; paulett.c.liewer@jpl.nasa.gov
[2] Johns Hopkins University Applied Physics Laboratory, Laurel, MD, 20723, USA
[3] Department of Physics, Montana State University, Bozeman, MT, 59717, USA
[4] Advanced Heliophysics, Pasadena, CA 91106, USA
[5] George Mason University, Fairfax, VA 22030 USA
*Received 2023 March 5; revised 2023 March 26; accepted 2023 March 27; published 2023 May 3*

## Abstract

Parker Solar Probe (PSP) crossed the heliospheric current sheet (HCS) near the perihelion on encounters E8 and E11, enabling the Wide-field Imager for Solar Probe (WISPR) to image the streamer belt plasma in high resolution while flying through it. With perihelia of 16 $R_\odot$ and 13 $R_\odot$ for E8 and E11, respectively, WISPR images enable investigation of the structure of density encasing the HCS at much higher resolution than reported previously. As PSP flies closer to the Sun, fine-scale structures are resolved within the coronal rays of the streamer belt. Near the HCS, WISPR observes a fan of rays of various sizes and brightnesses, indicating large density variations in the HCS plasma sheet transverse to the radial direction. Near the perihelion, when PSP's speed exceeds the solar corotation speed, some rays exhibit large changes in *apparent* latitude as the HCS is encountered, and rays pass over and under the spacecraft. The multiple viewpoints provided during the HCS crossing enable us to extract the coordinates of a few rays in a heliocentric frame. The rays were found to lie near the HCS from a PFSS model. We compare their locations to the location of the streamers as seen in synoptic maps from the Large Angle and Spectrometric Coronagraph, and find that the rays generally fall within the bright streamer bands seen in these maps, which confirms that they are features of the streamer belt plasma. We speculate that the density variations in the helmet streamer plasma result from continuous interchange reconnection along the coronal hole boundaries.

*Unified Astronomy Thesaurus concepts:* Solar coronal streamers (1486); Solar K corona (2042)

*Supporting material:* animations

## 1. Introduction

Beginning in late 2018, the Wide-field Imager for Solar Probe (WISPR; Howard et al. 2019) has been returning coronal images of unprecedented resolution during Parker Solar Probe's (PSP) encounter phases, that is, when the spacecraft is inside 0.25 au (Howard et al. 2022 and references therein). WISPR consists of two white light telescopes, an inner and outer. The field of view (FOV) of the inner telescope, WISPR-I, extends from 13.°5 to 53.°0 from the Sun, and the FOV of WISPR-O extends from 50.°5 to 108.°5 (Vourlidas et al. 2016). Images of the streamer belt from PSP's first encounter, with a perihelion of 0.17 au (36 $R_\odot$) were analyzed in detail by Poirier et al. (2020). Finer substructures not visible from 1 au were seen within the coronal streamers.

As the mission progresses, PSP perihelion is lowered by gravity assists from encounters with Venus (Fox et al. 2016). With decreasing distance to the Sun, WISPR's ability to resolve coronal features improves dramatically (Vourlidas et al. 2016; Howard et al. 2022). This is in part because the spacecraft is closer to the Sun and, more importantly, because WISPR's coronal images result from Thomson scattering of sunlight by coronal electrons. Most of the Thomson-scattered signal comes from a broad maximum around the Thomson surface, a sphere with the diameter of the Sun–PSP distance connecting the Sun and PSP, and thus, the region of sensitivity decreases proportionately as the perihelia shrink. For a coronagraph at 1 au, the integrated signal along a line of sight (LOS) may include contributions from many coronal streamers at a wide range of longitudes, but from inside 0.1 au ($<20\,R_\odot$), the integrated signal comes from a dramatically smaller region near the telescope (Vourlidas et al. 2016).

In 2021 February, PSP's fourth Venus gravity assist lowered the perihelion to $<20\,R_\odot$. At this distance, the inner edge of the WISPR field of view reaches down to 4 $R_\odot$, and the diameter of the Thomson surface is $< 0.1$ au (versus 1 au for coronagraphs in Earth's orbit). Thus, when PSP is this close to the Sun, WISPR is imaging only the local environment, providing unique data on the density structure of the corona (Vourlidas & Howard 2006).

Largely due to coronagraph images from the Large Angle and Spectrometric COronagraph (LASCO; Brueckner et al. 1995) and solar eclipses, coupled to magnetic field modeling, the general relationship between the quasi-stationary coronal streamers seen in coronagraphs and the magnetic structure of the corona has been established (Wang et al. 1997, 2000a and references therein). The large helmet streamers separate open magnetic field lines of opposite magnetic polarity and lie at the base of the heliospheric current sheet (HCS) and its surrounding plasma sheet. A fine ray-like structure was observed within the streamers. Pseudostreamers separate field lines of the same polarity and have plasma sheet, but not current sheet, extensions (Wang et al. 2007). In addition to the quasi-

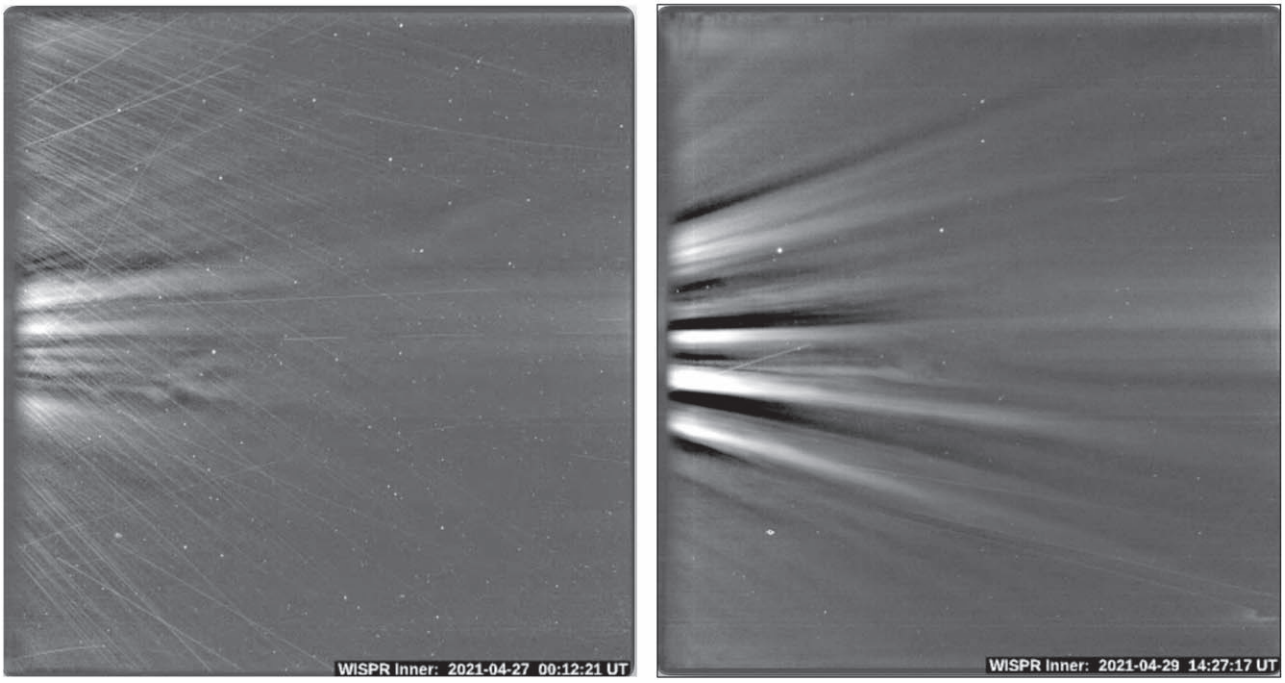


**Figure 1.** Two frames from the WISPR-I E8 animation, which illustrates the change in the appearance of the streamer belt as PSP approached the HCS near perihelion and the resolution increases. The movie covers the time period from 2021 April 27 0 UT to May 1 0 UT. The first movie frame (left image above) was taken from a distance of 30.5 $R_{\odot}$ and shows diffuse streamer belt structures. The right image above, taken from 16.3 $R_{\odot}$ on April 29 14 UT, shows that the the streamer rays have been resolved into much finer-scale rays of various sizes and brightnesses, indicating large transverse density variations in the HCS plasma sheet. The animation duration is 4 s.

(An animation of this figure is available.)

stationary streamers and pseudostreamers, polar plumes overlying bipoles in coronal holes are also visible in coronal images (Wang et al. 2007). Wang et al. (1998) suggested that magnetic reconnection between open and closed fields lines continually fed plasma onto the open field lines, thus creating the denser plasma of the streamers and leading to the filamentary appearance of the rays seen in both LASCO and eclipse observations.

To investigate the density variations in the HCS plasma sheet, Thernisien & Howard (2006) analyzed the structure of the plasma sheet in a large helmet streamer. LASCO had imaged the helmet streamer both "face-on" (telescope looking perpendicular to the HCS) and "edge-on" (telescope looking along the HCS). They used forward modeling to reproduce the two views to determine how the density varied along the plasma sheet. They found that the density along the HCS could vary by an order of magnitude. Decraemer et al. (2019) used simultaneous images from STEREO and LASCO to view the a helmet streamer "face-on" and "edge-on" and, again using forward modeling, found the density variations along the HCS of about a factor of 3.

LASCO images also showed a transient component in the streamer belt plasma. The streamer belt plasma near the HCS has small density enhancements, referred to as "blobs," moving at approximately the local solar wind speed (Wang et al. 2000b). With the advent of the two viewpoints provided by the Solar Terrestrial Relations Observatory (STEREO) (A) and (B), the Sun Earth Coronal Connection and Heliospheric Investigation (SECCHI; Howard et al. 2008) coronagraphs showed that these blobs were, in fact, small flux ropes, formed when helmet streamer loops reconnect with each other and pinch off (Sheeley et al. 2009; Rouillard et al. 2010).

From tracing in situ solar wind data back to the Sun using various potential-field source-surface (PFSS) models, streamer belt plasma was found to be denser than solar wind from coronal holes and much more variable. The composition of streamer belt plasma is similar to that of plasma in heated, closed magnetic loops, unlike that of wind from coronal holes (Zurbuchen et al. 2000 and references therein). This is consistent with the streamer belt plasma originating from interchange reconnection near coronal hole boundaries and reconnection at the tips of helmet streamers, where plasma from the heated, closed loops can be released onto the newly open field lines.

In this paper, we investigate the structure of the plasma near the HCS from WISPR's unique perspective: inside the streamer belt. We present the results of the analysis of WISPR's encounters with the HCS in encounters 8 and 11 (E8 and E11, hereafter). In both encounters, PSP crossed the HCS near the perihelion (16 and 13 $R_{\odot}$ for E8 and E11, respectively), enabling an investigation of the structure of density encasing the HCS at higher resolution than reported previously (Poirier et al. 2020). As PSP flies closer to the Sun, finer-scale structure is resolved within the rays of the streamer belt. Near the HCS, WISPR observes a highly resolved fan of bright rays of varying sizes and brightnesses, indicating large variations in the HCS plasma sheet density transverse to the radial direction, as illustrated in Figure 1. This is consistent with the above cited results of Thernisien & Howard (2006).

Near the perihelion, there is a period of time when PSP's speed exceeds the solar rotation speed. During this super-rotation period, WISPR images the fine-scale rays as PSP flies through them. As the distance between WISPR and a streamer with fixed latitude decreases, the *apparent* latitude of the

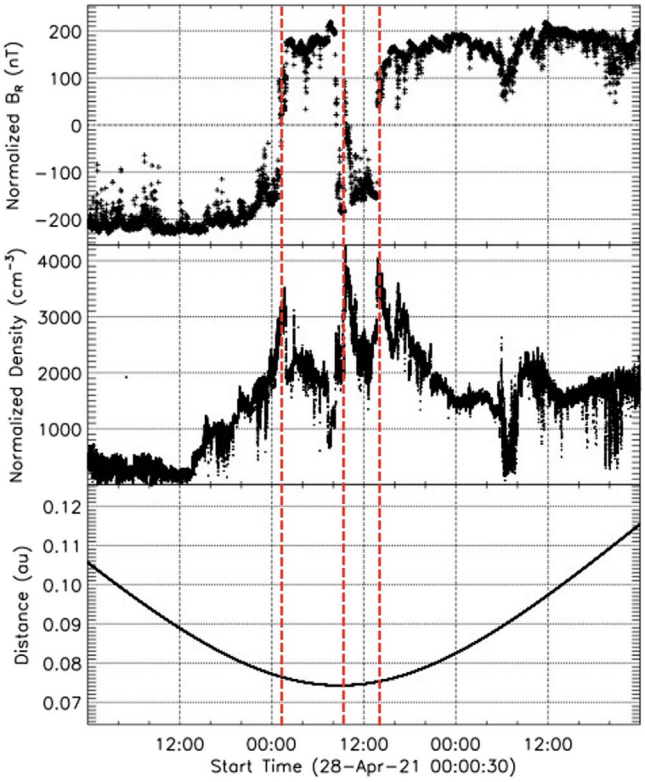


**Figure 2.** Plots of PSP in situ data for 3 days around the E8 perihelion. The top plot is the radial component of the magnetic field, showing the three closely spaced HCS crossings on April 29. The middle plot is the density, showing three density spikes coincident with the three HCS crossings. To remove the radial dependence, both quantities are normalized by $(R_P/R_P(0))^2$ where $R_P$ is the distance between PSP and the Sun, and $R_P(0)$ is the distance at the start time of the plot. The lower panel shows the PSP-Sun distance.

streamer will increase or decrease until WISPR passes over or under it. The WISPR data shows that many rays exhibit these large changes in apparent latitude as the HCS is crossed, which we interpret to result from the fly-through. As PSP flies through the streamer belt, the multiple views of distinct rays, specifically the rate of change of the apparent latitude, allow us to extract their coordinates in a heliocentric frame under the assumption that the rays are stationary and radial in a heliocentric coordinate frame. This technique, described in Liewer et al. (2022; hereafter Paper I), was used to extract the coordinates for a few distinct rays in both E8 and E11.

In E8, WISPR also imaged a variety of small transient blobs. For two of these that could be seen in a long enough series of images, we extracted the trajectories using the technique described in Liewer et al. (2020), which assumes that the blobs move radially at a constant velocity in a heliocentric coordinate frame. This technique, like the closely related technique for extracting ray coordinates, also uses the multiple viewpoints of the feature enabled by PSP's rapid speed to extract the trajectory.

We find that, for both encounters, the ray coordinates extracted lie near the HCS as predicted by a PFSS model (Badman et al. 2020, 2022). For E8, the extracted blob coordinates also lie near the HCS. All extracted coordinates fall on or near bright bands of LASCO/C3 synoptic maps. Since these bright bands show the structure of the coronal streamers at a given height, this confirms that the tracked features are situated in the streamer belt plasma encasing the HCS. The E8 blobs also fall on the HCS, and thus are consistent with origin near the tip of the helmet streamer. In addition, for E8 and E11 rays, we traced their locations down to $1.2\,R_\odot$ using a PFSS model and find they originate at the boundaries of polar coronal holes.

The paper is organized as follows: Section 2 presents the context, observations, and analysis of the E8 encounter with the HCS, including both the extracted coordinates for several bright rays, the extracted trajectories of two blobs, and a comparison of the results with LASCO observations. Section 3 presents the context, observations, and analysis of the E11 HCS encounter, including the extracted coordinates for two bright rays and a comparison with LASCO observations. In Section 4, the results are presented for the determination of the source of both E8 and E11 rays using PFSS models. Section 5 gives a summary and discussion and speculations about the processes leading to the observed narrow ray-like structures and large density inhomogeneities in the HCS plasma sheet.

## 2. E8 Encounter with the Heliospheric Current Sheet

PSP's eighth encounter with the Sun followed the fourth Venus gravity assist, which reduced the perihelion from 20.3 to $15.9\,R_\odot$. E8's perihelion occurred on 2021 April 29 at 9 UT. On this same day, the magnetometer in the FIELDS instrument suite (Bale et al. 2016) showed three closely spaced HCS crossing between 4 and 13 UT. The measured radial magnetic field, the density measured by the Solar Wind Electrons Alphas and Protons (SWEAP) Investigation (Kasper et al. 2016), and PSP's distance to the Sun are plotted in Figure 2 for 3 days around the perihelion, April 28–30. To remove the dependence on Sun–PSP distance, the values of the electron density and radial magnetic field are normalized by $(R_P/R_P(0))^2$ where $R_P$ is the distance between PSP and the Sun, and $R_P(0)$ is the distance at the start time of the plot. Note that three density peaks are coincident with the three HCS crossings, indicated by the three dashed red lines in Figure 2. PSP is in a region of enhanced density for all of April 29.

Figure 3 is a Carrington plot (heliographic latitude versus Carrington longitude) of PSP's orbit (solid line) covering the E8 period with one *tick* per day. The orbit *loop*, from April 27 to May 2, occurs when PSP is moving faster than the Sun rotates, and, here, PSP's Carrington longitude increases with time. Also plotted is the HCS calculated from a PFSS magnetic field model that best matches the measured magnetic field polarity (Badman et al. 2020, 2022), generated using `{pfsspy}` (Stansby et al. 2020) and GONG-ADAPT magnetograms (Arge et al. 2010). This PFSS shows a single, oblique HCS crossing on April 29 at about 12 UT and not the three crossings observed. The measurements reveal a more complex, possibly folded current sheet than can be captured by the PFSS model. In any case, the model HCS lies quite close to the orbit for the period of time when the three HCS crossings were observed, and thus, it is probably a reasonable estimate of the location of the HCS. This figure also shows the slight, approximately 4°, inclination of PSP orbit plane to the solar equatorial plane. The colored symbols are the coordinates extracted for various streamer belt features, which will be discussed below.

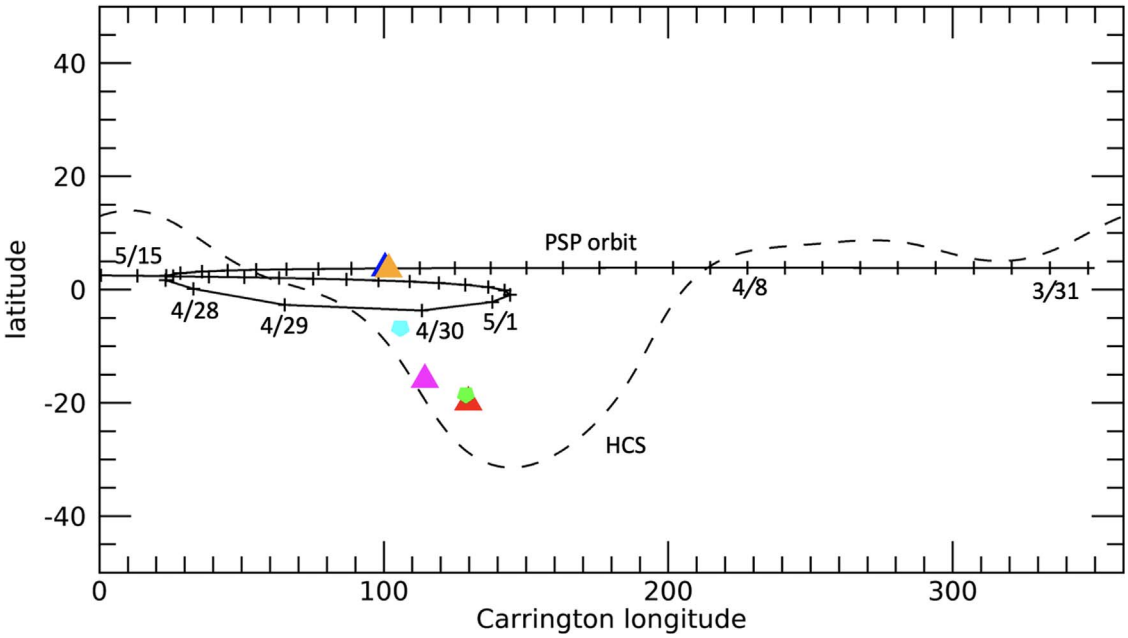


**Figure 3.** Carrington plot of PSP's orbit (solid line with one tick per day) covering the encounter period. The orbit *loop*, from April 27 to May 2, occurs when PSP is moving faster than the Sun rotates, and thus, PSP's Carrington longitude increases with time. Also plotted is the HCS (dashed line) calculated from a PFSS model. The colored symbols mark the extracted coordinates of various features, discussed below.

### 2.1. WISPR Observation during E8

As PSP approached the perihelion and the HCS in E8, WISPR images resolved the streamer belt plasma into a fan of fine-scale rays of varying sizes and brightnesses. The dramatic increase in resolution is evident in Figure 1, which shows images from WISPR-I, the inner telescope, at two times. The left image was taken from a distance of 30.5 $R_\odot$ on April 27 at 0 UT, and the right image was from 16.3 $R_\odot$ on April 29 at 14 UT. The approximate factor of 2 decrease in Sun–PSP distance has nearly doubled the angular size of the Sun. The inner edge of WISPR's FOV, fixed at 13.°5 from the Sun center, has moved inward from 7 to 4 $R_\odot$, and the Thomson sphere has shrunk to approximately half the size it was at 30.5 $R_\odot$. Both factors contribute to the dramatic increase in WISPR's resolving ability. The right image from 16.3 $R_\odot$ shows a much-finer-scale structure in the streamer rays compared to that from the left image from 30 $R_\odot$. The animated version of Figure 1 shows the resolution into finer and finer structures as the spacecraft flies close to the Sun and the changes in the apparent latitude of rays as PSP crosses the HCS. The large changes in apparent latitude are indicative of PSP flying through the quasi-stationary structures of the streamer belt. WISPR has resolved the streamers into much-finer-scale rays than previously observed, indicating that the density of the HCS plasma sheet is highly variable in the direction transverse to radial.

The resolution of the coronal streamers into rays of finer and finer scales with decreasing distance to the Sun is best seen in lat-maps, which show latitude versus time for a fixed solar elongation (Poirier et al. 2020; Nindos et al. 2021). Lat-maps are related to the better-known J-maps, which show the reverse: elongations versus time for a fixed latitude. Figure 4 illustrates how the lat-maps in this paper are created. The WISPR image shown, for April 29 at 14:27 UT, is a projection of both inner and outer telescopes' images into the observer-centric PSP orbit frame. In this frame, the latitude is measured from the PSP orbit plane (blue line), and the lines of constant solar elongation are Sun-centered circles. PSP's orbit plane is essentially the same as Venus' and inclined to the solar equatorial plane by ≈4°. In the image, the Sun is shown to scale. To make a lat-map, the data for a fixed range of elongation for all latitudes for each image in a time sequence is collected, reformed into strips; and the strips are stacked in time to show the temporal evolution at this elongation. The two Sun-centered blue circles in Figure 4 are at elongations of 24° and 26° and show the data to be used in a lat-map for this elongation range. The resulting lat-map is shown in Figure 5. In this figure, the data taken from the WISPR image in Figure 4 is outlined in white. This map shows the temporal evolution in the elongation range 24°–26°. Note that the lat-map has three axes on the bottom—time, PSP-Sun distance $R_P/R_\odot$, and PSP's Carrington longitude—to facilitate a comparison with the information in Figures 2 and 3. The red arrow on the lat-map indicates the period of superrotation, the time period in which PSP's speed exceeds the solar rotation speed. At a given time, the distance from the Sun to the Thomson sphere $R_T$ is the same for all data with the same elongation $\epsilon$, given by $R_T = R_P \sin(\epsilon)$, where $R_P$ is the distance from the Sun to PSP. This map and the WISPR image in Figure 4 were made using the level (3) (L3) processed data. Briefly, L3 images have the F-corona background removed and are calibrated in units of solar brightness. The procedure for creating the L3 images is described in detail in the Appendix.

Referring to the WISPR-I lat-map in Figure 5, it can be seen that, as PSP goes from 35 to about 18 $R_\odot$, more and more structure is resolved. Then, as PSP encounters the HCS crossings on April 29 and flies through the structures, the apparent latitude of many rays changes dramatically. Some can be seen to leave the FOV. Some individual rays persist as PSP changes its view point by 20° or more of Carrington longitude, indicating these features are not an LOS effect. (A streamer fly-through made using simulated WISPR observations can be found in the supplementary material to Liewer et al. 2019.) The rays become fainter as PSP moves farther from the Sun,

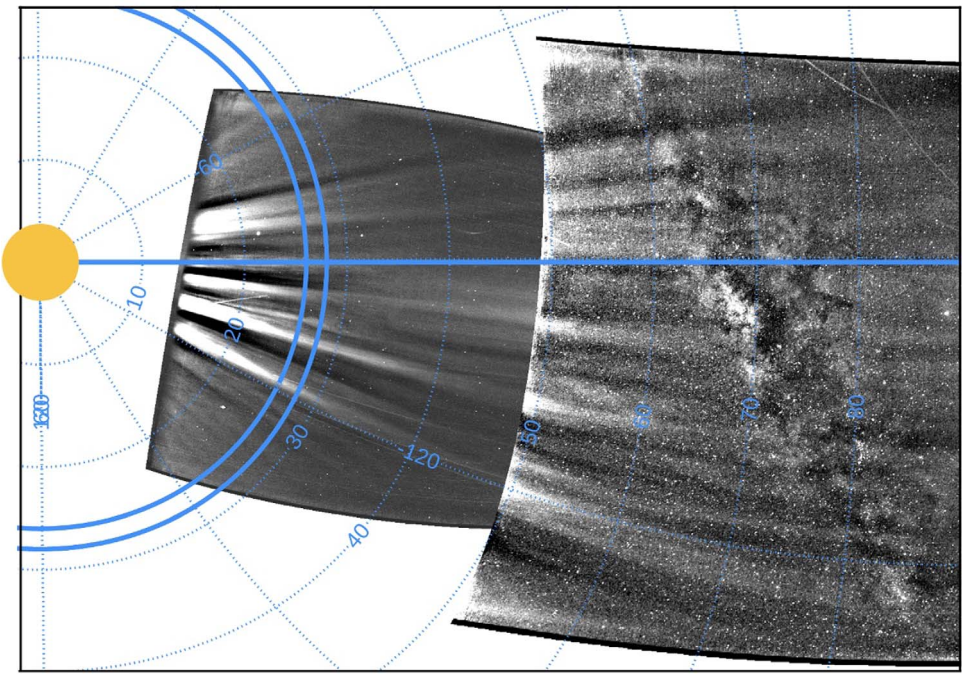


**Figure 4.** WISPR-I and -O images for April 29 at 14:27 UT combined and projected into the observer-centric PSP orbit frame in which 0° latitude (straight blue line) is the PSP orbit plane. The two circles centered on the Sun are placed at 24° and 26° elongation from the Sun center and illustrate the date selected from this image used in making the lat-map in Figure 5. The Sun is shown to scale in size and distance. See text.

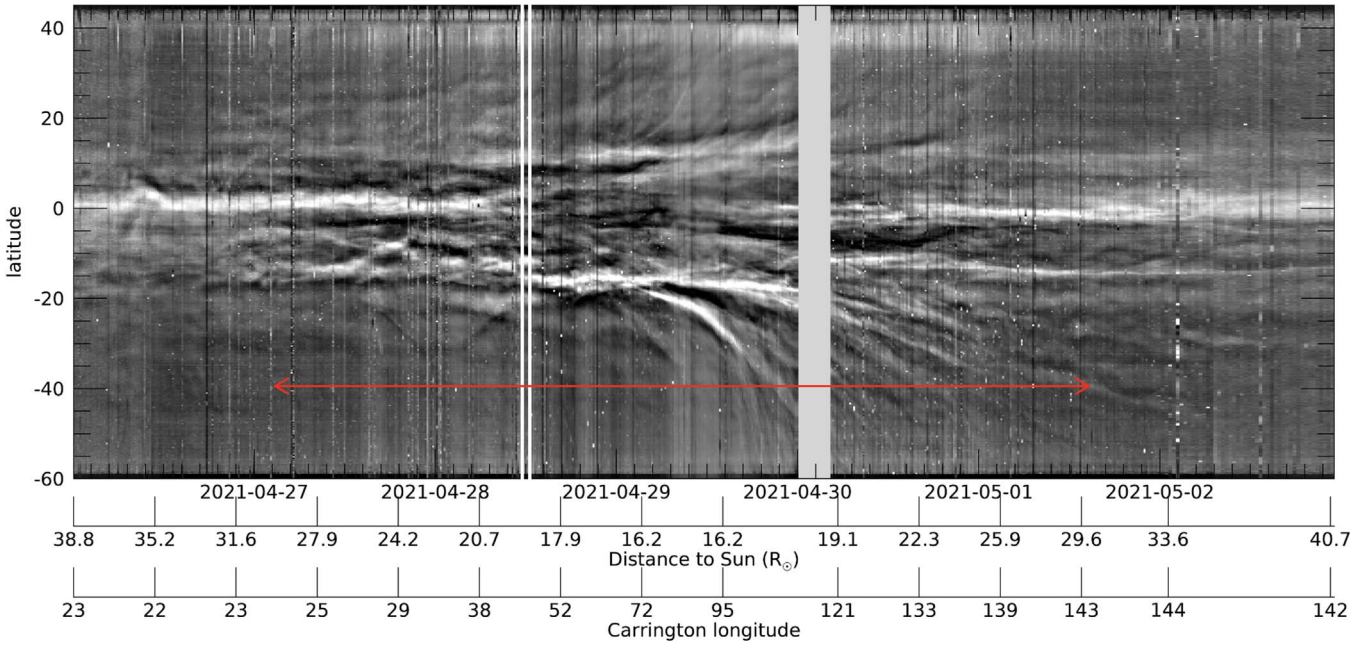


**Figure 5.** E8 lat-map made from WISPR-I images for elongation range 24°–26° showing temporal evolution in latitude at this elongation from 2021 April 26 to May 3. The red arrow marks the superrotation period, when PSP was moving faster than the solar rotation rate. The rapid apparent change in latitude of some rays is apparent at the time of the HCS crossings on April 29. See text.

reaching 30 $R_\odot$ on May 2. An E8 WISPR-O lat-map for the elongation range 56°–58° is shown in Figure 6, covering the same period of time as the WISPR-I lat-map in Figure 5. The superrotation period is indicated with a red arrow. Fine-scale rays are resolved as PSP approaches the perihelion, and during the HCS encounter, the large changes in apparent latitude are again evident.

WISPR images of the streamer belt have also shown that the resolved rays have fine-scale density variations *along* the rays. Figure 7 shows two WISPR-I images for the same time, but processed differently. On the left is the standard L3 processed image. The image on the right was made using a processing that enhances the changes in the images from frame to frame, termed "LW" processing, which is described in the Appendix to Howard et al. (2022). It can be seen that every bright ray has a small-scale variability in brightness, indicating a variable density, in the radial direction. Thus, the coronal streamers vary in density both in the radial and transverse directions. Such

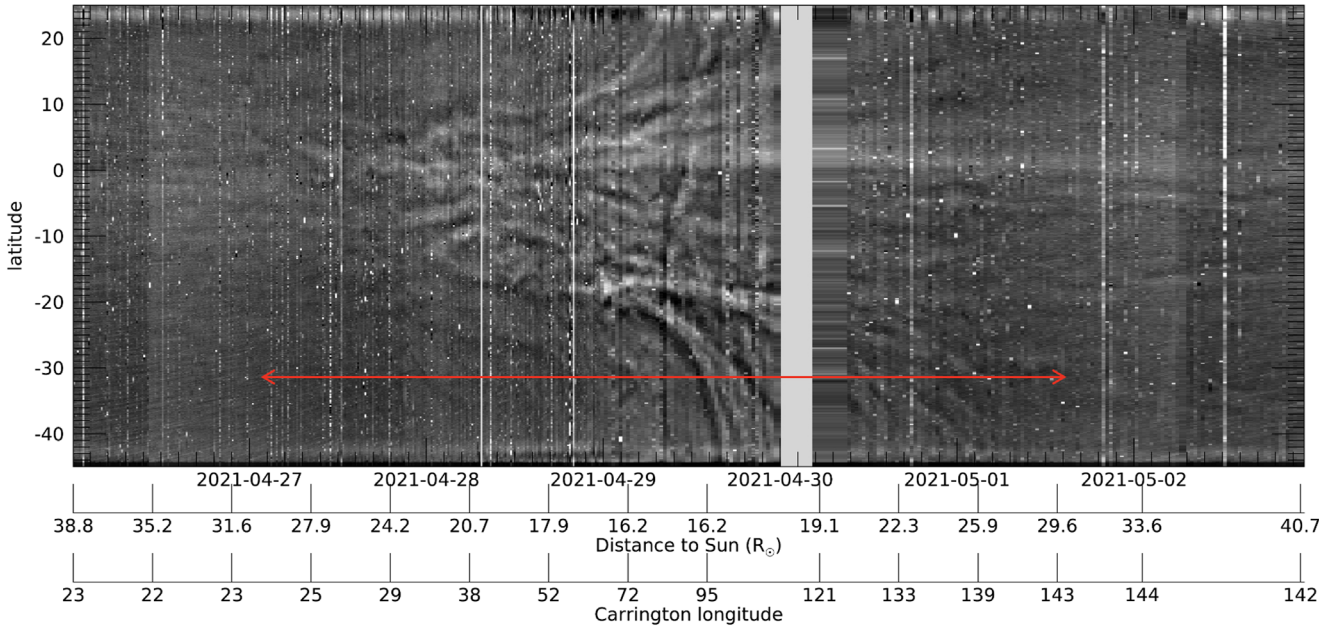


**Figure 6.** E8 lat-map made from WISPR-O images for elongation range 56°–58° showing temporal evolution at this elongation from 2021 April 26 to May 3. The red arrow marks the superrotation period, when PSP was moving faster than the solar rotation rate. Multiple streamers are resolved, and large apparent changes in latitude are seen as PSP crosses the HCS on April 29.

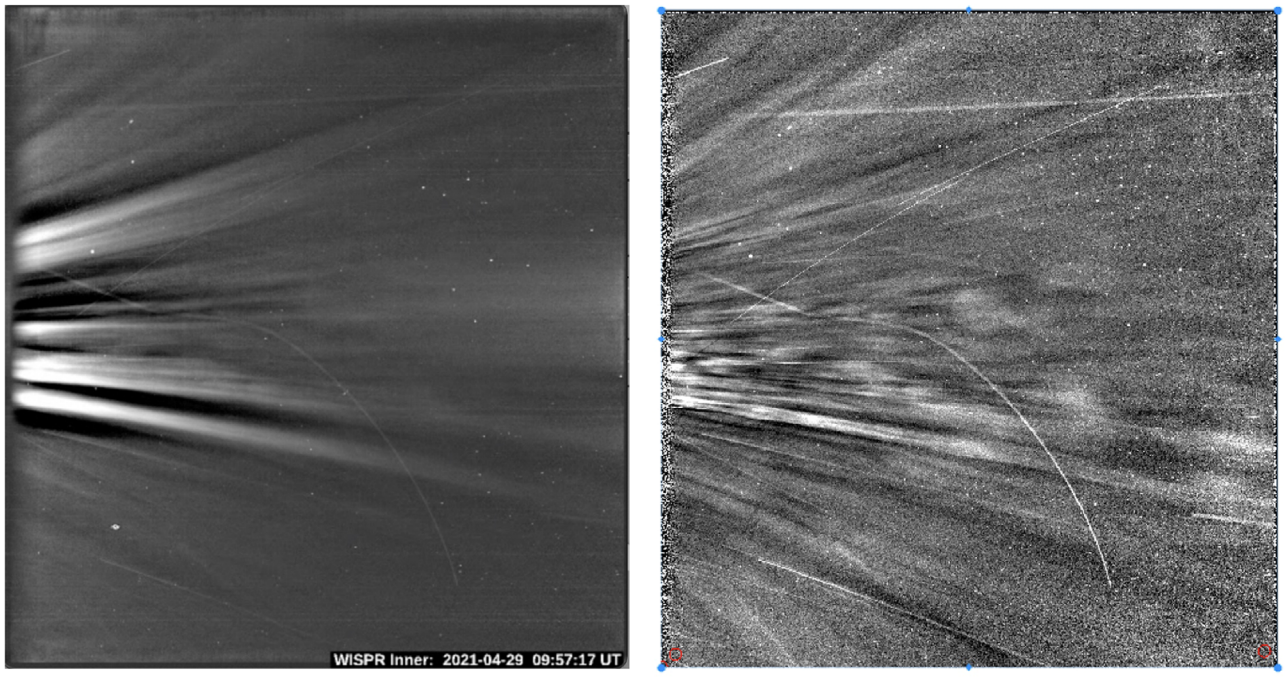


**Figure 7.** Two WISPR-I images, both for the same time (2021 April 29 at 9:57 UT), but processed differently. The image on the left is the L3 processing with calibrated brightness (see Appendix). The right image is processed using an image-differencing process, which enhances the changes from image to image, named LW processing (see Appendix to Howard et al. 2022). Using this processing, the very small variations in density along the rays are revealed.

striated flows and density variations were also found in E10 in the outflow behind a coronal mass ejection (Howard et al. 2022) and are reminiscent of the coronal images in DeForest et al. (2018). The cause of the observed radial density variations has not yet been investigated.

### 2.2. Extraction of Ray Coordinates

Paper I demonstrated a technique for extracting the coordinates of quasi-stationary coronal streamer rays using WISPR images from PSP's E7 encounter with the HCS. The technique assumes that the rays are radial in a heliocentric coordinate system [heliocentric inertial (HCI) or Carrington (CAR)] and makes use of the multiple viewpoints of the same feature to extract its latitude and longitude. We summarize the tracking and fitting technique here. Once it is determined that a ray can be identified in a sufficiently long series of images, a small number points along the chosen ray are selected manually using a cursor at each time (each image) in the sequence. This results in a tracking data set for that ray. Using the assumption

**Table 1**
Summary of Results for Determination of Ray Coordinates for E8

| E8 Coronal Ray | WIS-I L3 bright low | WIS-I LW thin high | WIS-O L3 high | WIS-O L3 low |
|---|---|---|---|---|
| Assigned color | Red | Blue | Orange | Magenta |
| Tracking start time | 2021-4-29T06:12 | 2021-4-29T03:57 | 2021-4-29T01:04 | 2021-4-29T09:04 |
| Tracking end time | 2021-4-29T13:12 | 2021-4-29T08:12 | 2021-4-29T04:34 | 2021-4-29T16:04 |
| **CAR frame** | | | | |
| Longitude (°) | $129.7 \pm 1.1$ | $100.4 \pm 1.2$ | $101.7 \pm 2.6$ | $114.4 \pm 0.6$ |
| Latitude (°) | $-19.9 \pm 0.3$ | $3.8 \pm 0.3$ | $3.6 \pm 0.5$ | $-15.9 \pm 0.3$ |
| Reduced $\chi^2$ | 2.2 | 0.1 | 0.2 | 1.0 |
| Radial extent ($R_\odot$) | 4–13 | 4–13 | 12–24 | 12–22 |
| **HCI frame** | | | | |
| Longitude (°)So | $121.4 \pm 1.1$ | $87.7 \pm 1.3$ | $88.4 \pm 2.9$ | $106.6 \pm 0.7$ |
| Latitude (°) | $-21.0 \pm 0.2$ | $4.9 \pm 0.4$ | $4.6 \pm 0.5$ | $-18.4 \pm 0.3$ |
| Reduced $\chi^2$ | 1.6 | 0.1 | 0.2 | 0.80 |
| Radial extent ($R_\odot$) | 4–14 | 5–12 | 13–30 | 12–27 |
| **Uncertainty in coordinates** | | | | |
| Error in longitude (°) | ±3.8 | ±2.7 | ±2.5 | ±3.3 |
| Error in latitude (°) | ±0.6 | ±0.6 | ±0.7 | ±1.3 |

**Note.** A ray's assigned color is used for identifying that ray in the various plots and figures.

that points along the ray have the same true latitude and longitude, analytic expressions were derived for relating the location of a point in the image at a given time to its location in a heliocentric frame, and for how the location of a point on the ray should change in the image as the location of PSP changes in time. The tracking data are fit to these analytic expressions to determine the latitude and longitude of the ray in either the Carrington or HCI frame; the same tracking data set can be used for both solutions. The points from a single image are used to define uncertainties in the measurements, which are then used in the fitting and calculation of the $\chi^2$ for the fit. While the spacecraft crosses more than 24° of Carrington longitude during a tracking (see Figure 5), the time is a matter of hours, and we cannot determine which solution, Carrington or HCI, is a better fit to the data (Paper I). Instead, we use the difference in the two solutions as an estimate of the uncertainty in the result. The reader is referred to Paper I for the details of the technique, the errors, and the validation tests.

For E8, two rays were tracked in WISPR-I images, which can be seen in Figure 5: the lowest very bright ray with the largest apparent latitude change at the perihelion and a very faint, narrow higher ray, which could only be tracked using LW processed images. Two rays were also tracked in the outer telescope using WISPR-O L3 images. Both can be seen in the lat-map from WISPR-O (Figure 6): The bright ray disappears out the bottom of the FOV in the afternoon of April 29, and the fainter ray disappears out of the top of the FOV in the morning of April 29. Thus, PSP passed between these two rays.

The results of the tracking and fitting of the four E8 rays are summarized in Table 1. Each ray has been given a name, which also identifies the telescope whose images were used in the tracking (WISPR-I, abbreviated WIS-I, or WISPR-O, abbreviated WIS-O). The table includes the angular coordinates as determined from the tracking and fitting in both the HCI and Carrington (CAR) frames, the $\chi^2$ for the fits, and the overall error in the coordinates determined from the difference between the HCI and Carrington solutions as explained in Paper I. The method for determining the radial extent of the ray segment tracked is explained later in this section. It can be seen from the coordinates in Table 1 that the WIS-I LW high ray and the WIS-O L3 high ray are, in fact, different segments of the same ray, which has been tracked independently in the inner and outer telescope images. Thus, the ray extends at least from 5 to 30 $R_\odot$.

The extracted coordinates in the Carrington frame for the four rays tracked were plotted on the Carrington map in Figure 3, first introduced above. The rays' coordinates are shown as colored triangles using the colors assigned in Table 1. This figure shows the relation of the rays locations to PSP's orbit and the HCS from a PFSS model (Badman et al. 2020, 2022). Note that all four rays fall near the HCS, consistent with the location expected for helmet streamer rays. The plot also shows clearly that the spacecraft passed under the inner and outer upper rays (blue and gold, respectively) and over the inner and outer low rays (red and magenta, respectively). The cyan and green circles show the angular coordinates of blob trajectories, discussed in the next section.

Images of the two WISPR-I rays are shown in Figure 8. In both images, the Sun's angular size and distance are shown to scale. (The Sun's shape is somewhat distorted by the projection used to display the WISPR image, which corrects for the telescope optics, but which has here been extended beyond the telescope's FOV.) Once the angular coordinates of a ray are determined, we can calculate the 3D coordinates of points along the ray at any time during the tracking in either the HCI or Carrington frame. We can then project these points onto one of the WISPR images used in tracking to verify the result. The left image in Figure 8 shows the first ray, WIS-I bright low, in the WISPR-I L3 image for April 29 at 6 UT. The red symbols are the projections of points along this ray, calculated from the HCI solution from $R = 4$ to 13 $R_\odot$ in increments of 1 $R_\odot$. The projected points fall on the ray tracked, as they must if the solution is correct, and thus, the solution is verified. The right image in Figure 8 shows the second ray (WIS-I LW thin high) in the WISPR-I LW image for April 29 at 1 UT. The blue symbols are projections of points along this ray, calculated from the HCI solution from $R = 13$ to 20 $R_\odot$ in increments of 1 $R_\odot$. The projected points fall on the ray tracked, and thus, this

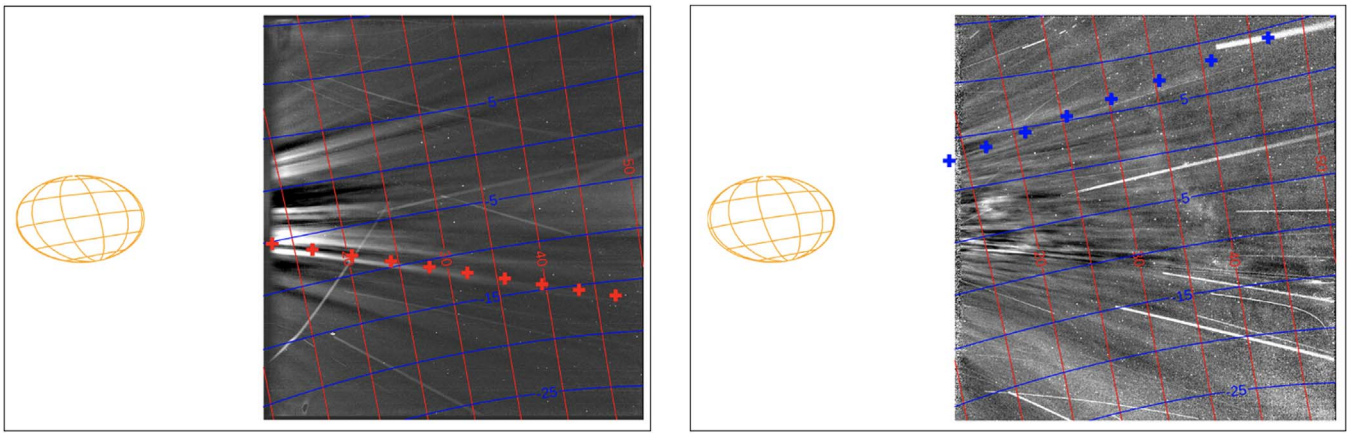

**Figure 8.** Images showing the rays whose coordinates were extracted from WISPR-I images. Left: WISPR-I L3 image for April 29 at 6 UT showing the WIS-I bright low ray. The red symbols are 3D points computed from the extracted coordinates, starting at 4 $R_\odot$ in increments of 1 $R_\odot$, which have been projected back onto the image. Right: WISPR-I LW image for April 29 at 3 UT showing the WIS-I thin high ray. The blue symbols are 3D points computed from the extracted coordinates, starting at 5 $R_\odot$ in increments of 1 $R_\odot$, which have been projected back onto the image. For both rays, the points fall on the rays tracked, thus verifying the solutions.

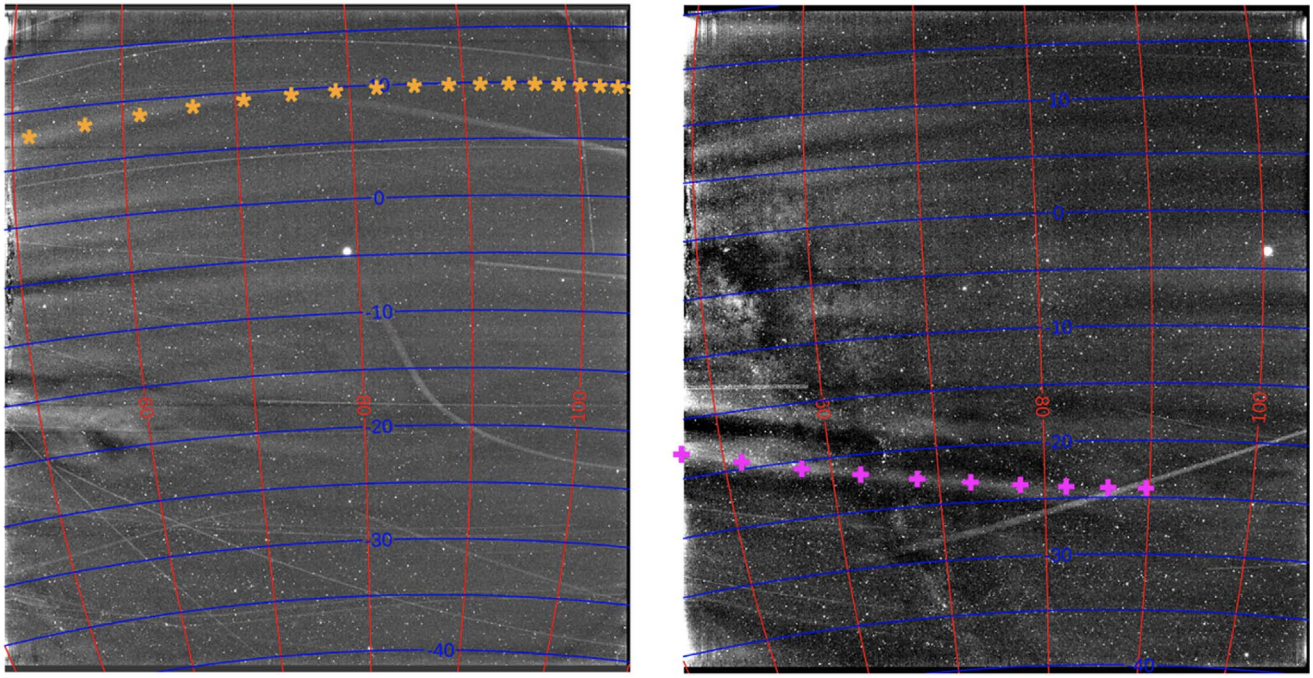

**Figure 9.** Images showing the rays whose coordinates were extracted from WISPR-O images. Left: WISPR-O image for April 29 at 01 UT showing the WIS-O L3 high ray. The gold stars are 3D points computed from the extracted coordinates, starting at 13 $R_\odot$ in increments of 1 $R_\odot$, which have been projected back onto the image. Right: WISPR-O image for April 29 at 9 UT showing the WIS-O L3 low ray. The magenta symbols are 3D points computed from the extracted coordinates, starting at 13 $R_\odot$ in increments of 1 $R_\odot$, which have been projected back onto the image. For both rays, the points fall on the rays tracked, thus verifying the solutions.

solution is also verified. Once verified, we also use these projections to determine the radial extent of the ray segment tracked, given in Table 1. The radial extent of the ray is determined by projecting points onto the first image used in the tracking, when the spacecraft is farthest away from the ray; the portion of the ray in the FOV decreases as PSP approaches the ray. (The *actual* extent of the ray likely much longer, of course.)

Images of the two WISPR-O rays are shown in Figure 9. In the left image, the ray WIS-O L3 high ray is shown in the WISPR-O image for April 29 at 10 UT. The orange stars are projections of points along this ray, calculated from the HCI solution from $R = 13$ to 29 $R_\odot$ in increments of 1 $R_\odot$. This ray was found to have nearly the same coordinates as the WIS-I thin high ray shown in Figure 8 and is thus considered to be the same ray, as discussed above. In the right image, the ray WIS-O L3 low ray is shown in the WISPR-O image for April 29 at 9 UT. The magenta symbols are projections of points along this ray, calculated from the HCI solution from $R = 13$ to 22 $R_\odot$ in increments of 1 $R_\odot$. For both rays, the projected solution falls on the ray tracked, thus verifying these solutions as well.

### 2.3. Extractions of Blob Trajectories

In WISPR's encounter with the HCS in E8, numerous transient density features or *blobs*, discussed in the Introduction, were also seen. Several were quite visible and can be seen in the animated version of Figure 1 online. The blobs could only be tracked in the LW processed images; only two of them

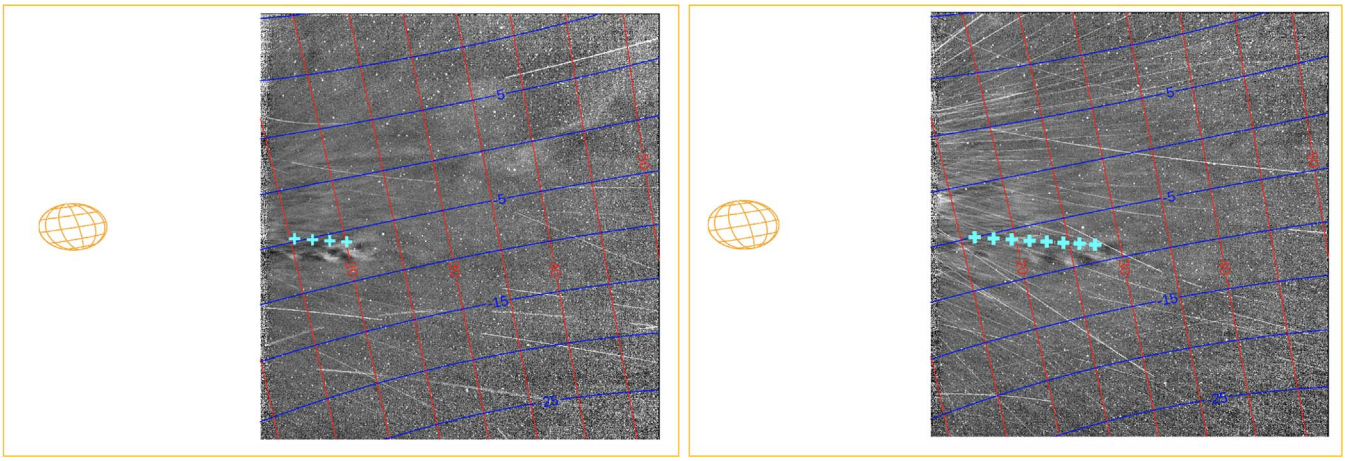

**Figure 10.** WISPR-I LW images showing the first blob at two times used in the tracking, April 27 at 11:43 UT (left) and April 27 at 02:42 UT (right). The cyan symbols are 3D points, calculated from the solution, projected back onto the WISPR image. The points start at the tracking start time, April 26 18:42 UT, and are plotted in 1 hr increments. In the image on the left, the last point plotted is at April 26 21:42 UT, 1 hr before the time of the image; the point for the time of the image is not plotted because it would obscure the tracked feature, the dark cavity in the leading blob. In the image on the right, the last point plotted is at April 27 at 01:42 UT, again 1 hr before the time of the image. Again, the point for the time of the image is not plotted because it would obscure the tracked feature itself.

were visible for a long enough time with sufficient spacecraft angular range to determine their 3D trajectory using the Tracking and Fitting technique, described in Liewer et al. (2020). This technique, closely related to the technique used to extract the coordinates of the rays, assumes that the blobs move in a radial line at a constant velocity in a heliocentric frame (again, HCI or Carrington) and relies on viewing the trajectory from multiple viewpoints to obtain a solution. The position of a *feature* of the blob is first tracked in a sequence of images, and the tracking data fit to analytic expressions to determine the four trajectory parameters: velocity, latitude, longitude, and distance from the Sun $R_0(t_0)$, where $t_0$ is the time that tracking began. Details can be found in Liewer et al. (2020).

The first blob is shown at two times in the WISPR-I LW images in Figure 10. It can also be seen in the left L3 images in Figure 1 and in the animated version of that figure. The images in Figure 10 are LW images used in the tracking. It was tracked from 2021 April 26 at 18:43 UT to April 27 at 08:13 UT. The feature tracked was the black cavity of the first of the three visible *knots*. The resulting solution was HCI longitude $= 61^\circ \pm 6^\circ$, latitude $= -17^\circ \pm 5^\circ$, velocity $= 190 \pm 6$ km s$^{-1}$, and $R_0(t_0) = 9.0 \pm 0.5\ R_\odot$. The position at the end of tracking was $R = 22.4\ R_\odot$. The errors were determined by comparing the solutions in the HCI and Carrington frames, as for the coronal ray solutions discussed in the preceding section [see also Liewer et al. 2020]. The extracted Carrington coordinates of this blob are plotted in Figure 3 as a cyan circle. In Figure 10, the Sun is again shown to scale. Note the smaller angular size here compared to the angular size in the WISPR-I images in Figure 8, obtained when PSP was much closer to the Sun.

With our knowledge of the trajectory parameters, we can calculate the 3D positions of the blob at any time during the tracking interval. We can then project these locations onto WISPR images and compare with the observed position of the blob to verify the solution, similar to the verification strategy used for the extracted ray coordinates. This has been done in Figure 10 for WISPR-I LW images at two times, April 26 at 22:42 UT (left) and April 27 at 02:42 UT (right). The earlier image on the left shows the projection of the solution points (cyan symbols) hourly at four times from $t_0$ (2021 April 26 at 18:43 UT) to 3 hr later, April 26 21:42 UT. The last point is 1 hr *before* the time of the image (April 26 at 22:42 UT). If we projected the point at the time of the image, it would obscure the dark cavity, the feature that was tracked. The later image on the right shows the projections of the solution points hourly for eight times from $t_0$ to 7 hr later, April 27 at 01:42 UT. Again, the last point projected is 1 hr before the time of the image because the point at the time of the image would obscure the dark cavity. Thus, our solution accurately falls on the blob's trajectory in both images, as it must if the trajectory solution is correct.

The second blob, shown at two times in the LW images in Figure 11, was tracked for 11.5 hr on 2021 April 27 from 10:13 UT to 21:43 UT. Here also, the feature tracked was the black cavity in the leading brightness enhancement. The resulting solution was HCI longitude $= 90.^\circ 6 \pm 6^\circ$, latitude $= -18^\circ \pm 1^\circ$, velocity $= 268 \pm 3$ km s$^{-1}$, and $R_0(t_0) = 9.2 \pm 0.5\ R_\odot$, where $t_0$ is the tracking start time. The position at the end of tracking was $R = 25.1\ R_\odot$. Again, to verify the solutions' parameters, we calculated trajectory points in 1 hr increments, starting at April 27 at 10:13 UT, the start time. The image on the left, taken April 27 at 11:43 UT, shows two trajectory points (green symbols). The image was taken 0.5 hr after the second point's time of 11:13 UT; this point falls behind the tracked feature, as it should. The image on the right shows eight hourly trajectory points, with the last at 17:13 UT, 7 hr after the start time. The image itself is from April 27 at 18:13, 1 hr later than the last point. The trajectory point at the time of the image is again not shown because it would obscure the feature tracked. So here also, the trajectory points calculated from our solution fall on the observed trajectory, verifying the solution. This blob can also been seen in the animated version of Figure 1.

The angular coordinates of the blob solutions were plotted as circles in Figure 3 in comparison with PSP's orbit and the HCS. The first (second) blob is plotted a cyan (green) circle, the same colors as in the figures showing the solution projections onto the WISPR-I images. Note that the locations are not only close to the HCS as expected for helmet streamer blobs but also close to the extracted coronal ray locations. (As discussed in the introduction, although blobs and some rays are associated with helmet streamers, they are thought to be

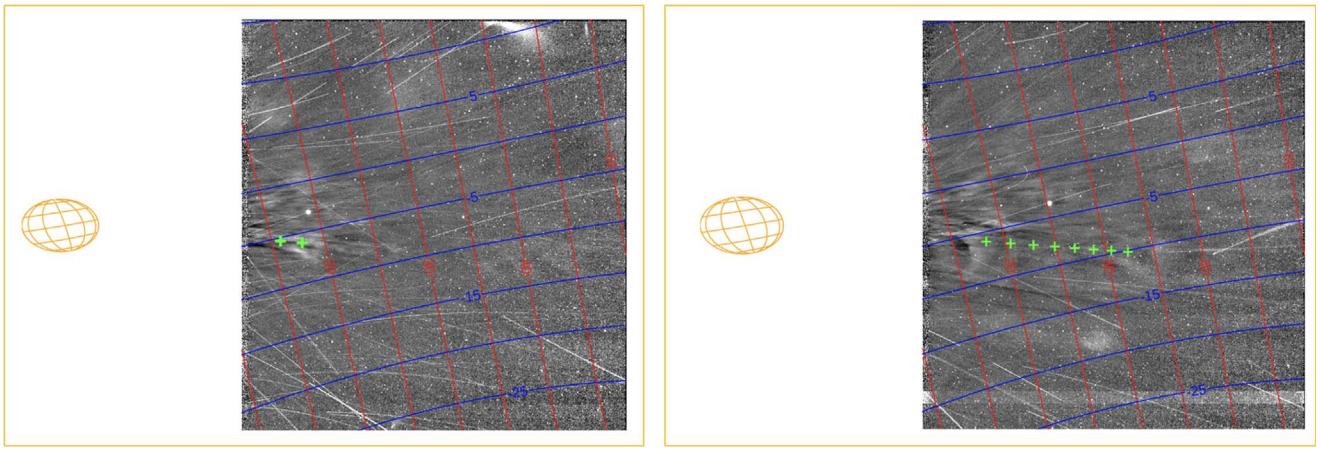

**Figure 11.** WISPR-I LW images showing the second blob at two times used in the tracking, April 27 at 11:43 UT (left) and April 27 at 18:13 UT (right). The cyan symbols are 3D points, calculated from the solution, projected back onto the WISPR image. The points start at the tracking start time, April 27 at 10:13 UT, and are shown in 1 hr increments. In the left image, the second point is at 11:13 UT, a half hour before the time of the image 11:43 UT. The point at the time of the image would obscure the featured tracked, the dark center of the leading blob. In the image on the right, the last point projected is at April 27 at 17:13 UT, which is 1 hour before the time of the image. Again, the point for the time of the image is not shown because it would obscure the tracked feature itself.

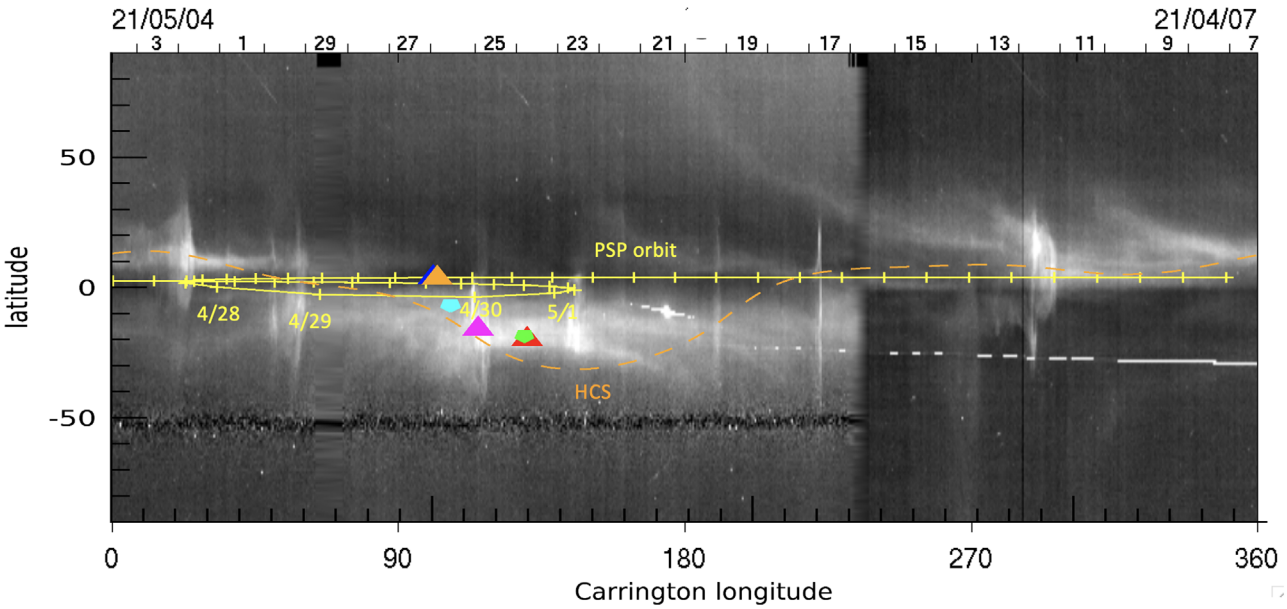


**Figure 12.** LASCO/C3 synoptic plot for Carrington rotation (2243) for the east limb at 10 $R_{\odot}$. The E8 PSP orbit, HCS, and extracted coordinates of the four rays and two blobs are displayed as in Figure 3. The ray coordinates are plotted as triangles using the colors assigned in Table 1. All features fall on or near the bright bands seen in the LASCO image, confirming that these features lie in the streamer belt. See text.

produced by different processes.) Although the ray and blob locations overlap in Carrington longitude range, the features were tracked during different time intervals. The blobs were tracked between April 26 at 18:43 and April 27 at 21:43 and were separated from the observed HCS crossing by more than 75°, whereas the rays were tracked later (see times in Table 1), when the spacecraft was flying through them during the HCS crossing. Thus, although tracked at different times and from different locations, our results show both types of features lie near the HCS. This is further confirmed in next section comparing the results with LASCO/C3 observations.

### 2.4. Comparison with LASCO/C3 Observations

In this section, we compare the results of the coordinate extraction for both rays and blobs with LASCO observations of the corona using the LASCO/C3 synoptic map covering the time period that the E8 rays were tracked. Coronagraphsynoptic Carrington maps are created in a manner analogous to synoptic magnetograms, but whereas for synoptic magnetograms, a solar rotation's worth of data are collected from the central meridian, for coronagraph maps; the data are collected from the limb for a specified height. Separate synoptic maps are created for the east and west limbs and for several different heights. LASCO synoptic maps are available at https://lasco-www.nrl.navy.mil/. As for synoptic magnetograms, the bottom axis is Carrington longitude, the $y$-axis is heliographic latitude, and the upper axis gives the date that the data for that longitude was collected. The image in Figure 12 is a LASCO/C3 synoptic map for Carrington rotation (2243) for the east limb at 10 $R_{\odot}$. Over this image, the Carrington coordinates of the tracked rays and blobs are plotted, as well as the PSP orbit loop (yellow line) and HCS (orange dashed line) from the PFSS model, as in Figure 3. Again, the rays are plotted as triangles in

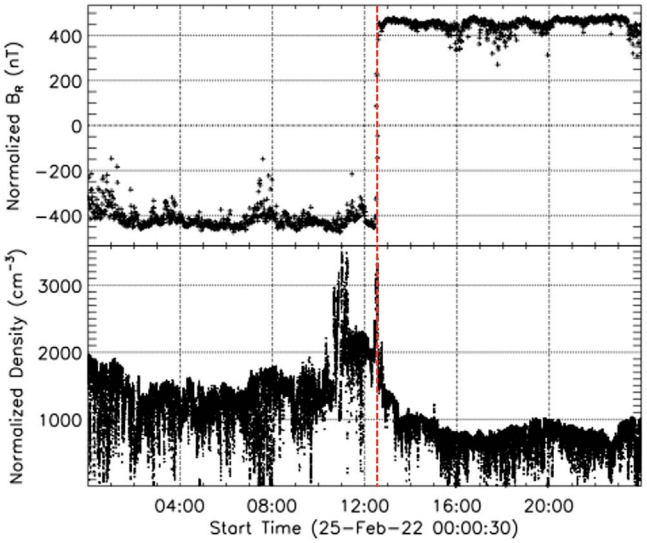


**Figure 13.** Plots of PSP in situ data for 2022 February 25. The top plot is the radial component of the magnetic field, which shows the quick, single HCS crossing close to the E11 perihelion on February 25 at 12:30 UT. The second plot is the density showing one spike at the crossings and another shortly before. To remove the radial dependence, both quantities are normalized by $(R_P/R_P(0))^2$, where $R_P$ is the distance between PSP and the Sun, and $R_P(0)$ is the distance at the start time of the plot.

the colors assigned in Table 1. The first and second blobs are plotted in cyan and green symbols, respectively, the same colors used in the projections in Figures 10 and 11. The bright bands in the LASCO/C3 maps show the location of the bright streamers. The brightest bands are generally associated with the helmet streamers and the HCS. It can be seen that the blobs and two of the rays fall within the brightest band, confirming their association with helmet streamers. The upper rays fall near, but not on, the brightest band.

## 3. E11 Encounter with the Heliospheric Current Sheet

E11, PSP's eleventh encounter with the Sun, followed the fifth Venus gravity assist in 2021 October, which reduced the perihelion from 15.9 to 13.3 $R_\odot$. The perihelion occurred on 2022 February 25 at 15:38 UT. On this same day, the magnetometer in the FIELDS instrument suite showed a single, quick HCS crossing at 12:30 UT, about 3 hr before the perihelion. The measured radial magnetic field component and the density measured by the SWEAP instrument suite are shown in Figure 13 for that one day. As in Figure 2, the values are normalized by $(R_P/R_P(0))^2$ where $R_P$ is the distance between PSP and the Sun, and $R_P(0) = 15.9\,R_\odot$ is the distance at the start time of the plot. Note that a very narrow density spike is coincident with the HCS crossing and a somewhat wider peak an hour before the HCS crossing. For E11, PSP is in a region of enhanced density for about 3 hr around the HCS crossing as compared to at least 24 hr in E8 (see Figure 2).

Figure 14 shows a Carrington plot of PSP's orbit, and as in Figure 3, we have plotted the HCS calculated from a PFSS model (Badman et al. 2020, 2022). The crossing predicted by the PFSS model is very close to the Carrington longitude of the observed HCS crossing at Carrington longitude = 109°.25 at 12:30 UT. This comparison of the HCS and the PSP orbit indicates that PSP crossed a nearly vertical HCS. Also plotted as colored triangles are the coordinates of two rays tracked during this HCS crossing, discussed below.

### 3.1. WISPR Observation for E11

As PSP approached the perihelion in E11, a finer and finer structure is resolved within the rays of the streamer belt, as in E8. Near the HCS, WISPR observes a highly resolved fan of fine-scale rays of varying size and brightness, again indicating large transverse density variations in the HCS plasma sheet. Figure 15 show three frames from the E11 animation covering February 22–27, made from L3 images. The left image was taken on February 22 at 0 UT when PSP was at 42.1 $R_\odot$, and the inner edge of the WISPR-I FOV was at 9.8 $R_\odot$. The center and right images are both taken on February 25, the day of both the HCS crossing and perihelion. For the center image, taken from 24.2 $R_\odot$ at 10:45 UT, the inner edge was at 5.6 $R_\odot$. For the right image, taken at 13.4 $R_\odot$ at the time of the HCS crossing, 12:30 UT, the inner edge reaches in to 3.1 $R_\odot$. The rays become brighter and better defined than those in the E8 images in Figure 1 because PSP is closer to the Sun. In the left and center images, the position of Venus is circled, and the dotted line approximates the PSP–Venus orbit plane. Note that, at the time of the HCS crossing (image on right), the brightest rays are seen below the orbit plane. In this encounter, WISPR's view of the HCS plasma sheet is *face-on* because the HCS is near vertical there (see Figure 13). Only faint rays are seen at the orbit plane, possibly due in part to the short LOS through the HCS plasma sheet as a result of the near-vertical HCS at the crossing.

The resolution of the rays into finer and finer scales as WISPR approaches the perihelion and the HCS is clearly seen in the WISPR-I lat-map shown in Figure 16. The construction of lat-maps was discussed above in Section 2.1; the super-rotation period is again indicated with the red arrow. As for E8, the lat-map is in the PSP orbit frame, so the latitude is measured relative to the orbit plane. Note the presence of a persistent diffuse bright band at the PSP–Venus orbit plane. This is due to Venus' dust ring, which was not removed in the L3 processing used for this orbit. This is explained in the Appendix describing the L3 processing procedure and the difference in the processing for E8 and E11. As PSP approaches the HCS crossing February 25 at 12:30 UT, the rays show the rapid increase in apparent latitude, indicating that PSP is flying though the coronal rays. A multitude of rays of various sizes of scales are resolved near the perihelion at 13.3 $R_\odot$, many more than in E8 (compare with Figure 5), as a result of the decrease in the perihelion and shrinking of the Thomson sphere and, thus, the region of sensitivity of WISPR. Many rays show the characteristic rapid change in apparent latitude as PSP flies through them. Note that the region closest to the orbit plane is lacking in bright rays, as noted in the discussion of Figure 15. This will be discussed further in the section below on comparison with LASCO synoptic maps.

A lat-map from WISPR-O is shown in Figure 17 for the elongation range 52°–54°. This covers a somewhat longer period of time than the WISPR-I lat-map in Figure 16. Note the many fine-scale rays with the decreases in apparent latitude as PSP flies over them during the superrotation period. In this lat-map, the Venus dust ring is especially visible, making it difficult to distinguish whether or not there are fine-scale rays near 0° latitude. Note that WISPR is still seeing rays with significant apparent latitude changes on February 26, well after the HCS crossing. Presumably, these are rays associated with the HCS that at that time was 40° or so below the orbit plane.

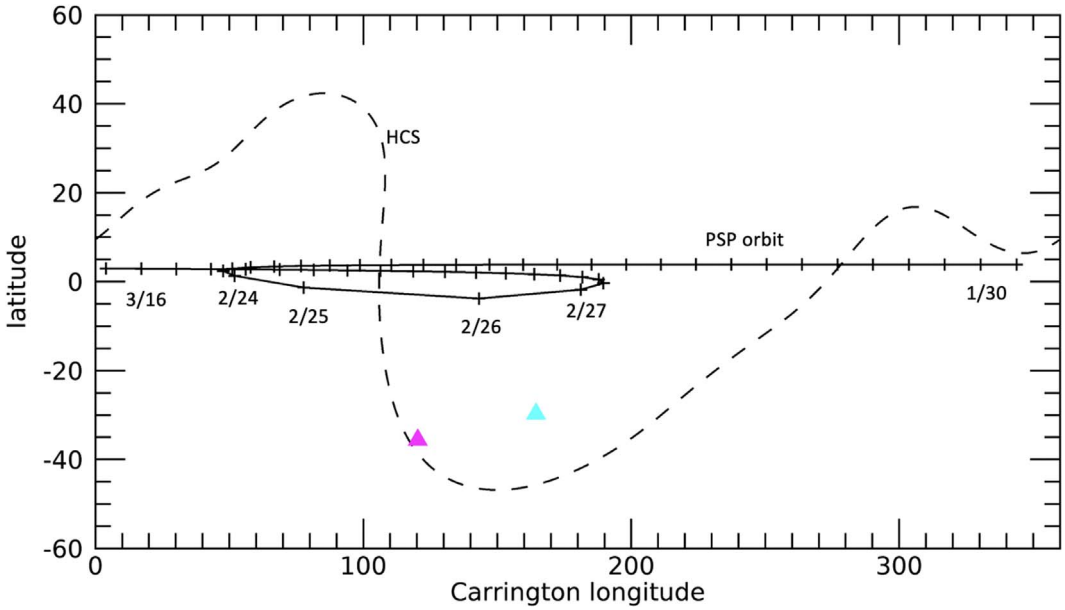


**Figure 14.** Carrington plot of PSP's orbit (solid line with one tick per day) covering the E11 encounter period. The orbit *loop*, from February 23 to 28, occurs when PSP is moving faster than the Sun's rotation, so PSP's Carrington longitude increases with time. Also plotted is the HCS (dashed line) calculated from a PFSS model. The colored symbols marked the extracted ray coordinates, discussed below.

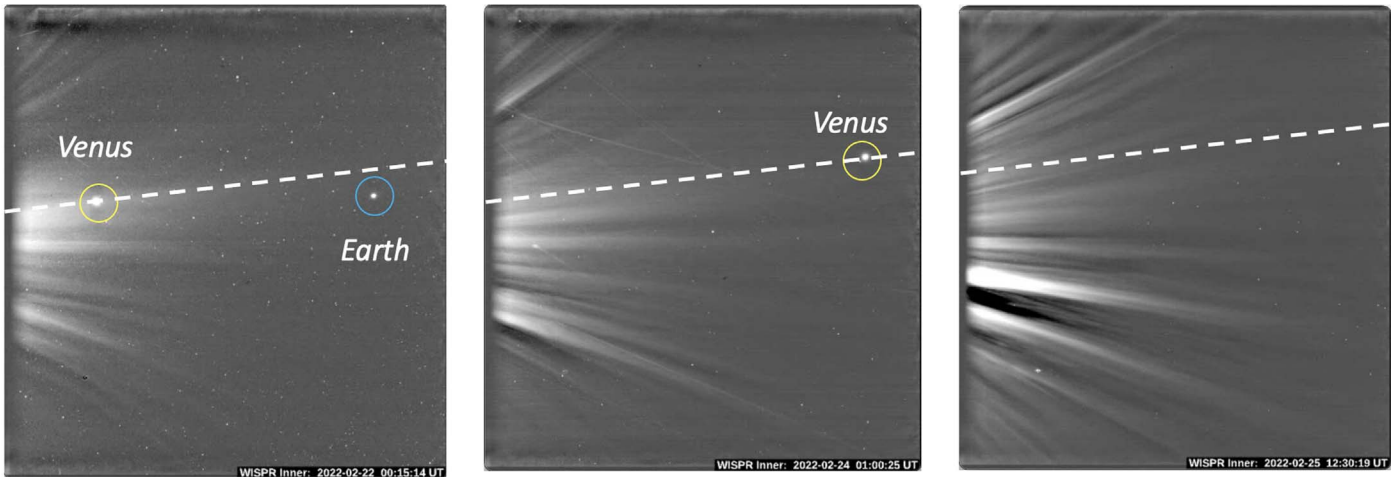


**Figure 15.** Three frames from the E11 WISPR movie, which shows how finer-scale structure is resolved within the rays of the streamer belt as PSP flies closer to the Sun. The movie, created from WISPR-I L3 images, covers the time period from 2022 February 22 at 0 UT to February 27 at 23 UT. The three frames shown above are from three distances as PSP encounters the HCS in E11. From left to right, the images are for February 22 at 0 UT and February 25 at 10:45 UT and 12:30 UT. The corresponding Sun–PSP distances are 42.1, 24.2, and 13.4 $R_{\odot}$. The image on the right, taken at the time of the HCS encounter, shows the that the coronal rays have been resolved into a fan of fine-scale rays of varying sizes and brightnesses. The dashed line approximates the PSP–Venus orbit plane. The animation real-time duration is 5 s.

(An animation of this figure is available.)

### 3.2. Extraction of E11 Ray Coordinates

In this section, the results for extracting the coordinates for two of the bright rays seen in Figure 16 are presented. The technique for determining the coordinates was discussed in Section 2.3. The information regarding the solutions for the two E11 rays tracked is summarized in Table 2, presented in the same format as Table 1, and discussed in Section 2.2.

The ray WIS-I February 24, identified with the magenta arrow in Figure 16, is shown in the left image of Figure 18, the WISPR-I L3 image from February 24 at 15 UT. We generate points along this ray from the HCI solution and project them back onto an image used in tracking to verify the solution, as was done for the E8 rays. In the left image of Figure 18, the points start at 5 $R_{\odot}$ and are placed in increments of 1 $R_{\odot}$. Thus, the length of the segment in the WISPR-I FOV at the start of tracking is 11 $R_{\odot}$. The projected points fall on the tracked ray, confirming the solution from tracking and fitting.

The ray WIS-I February 25, identified in Figure 16 with the cyan arrow, is shown on the right in Figure 18, the WISPR-I L3 image from February 25 at 10 UT. As for the other rays, using the coordinates from the HCI solution, we generate points along the ray, then project them back onto the image used in tracking to verify the solution. For this figure, the points start at 3 $R_{\odot}$ and are plotted in 1 $R_{\odot}$ increments. Thus, the length of the segment in the WISPR-I FOV at the start of tracking is 10 $R_{\odot}$. Again, the projected ray points fall on the tracked ray, confirming the solution from tracking and fitting. Note the

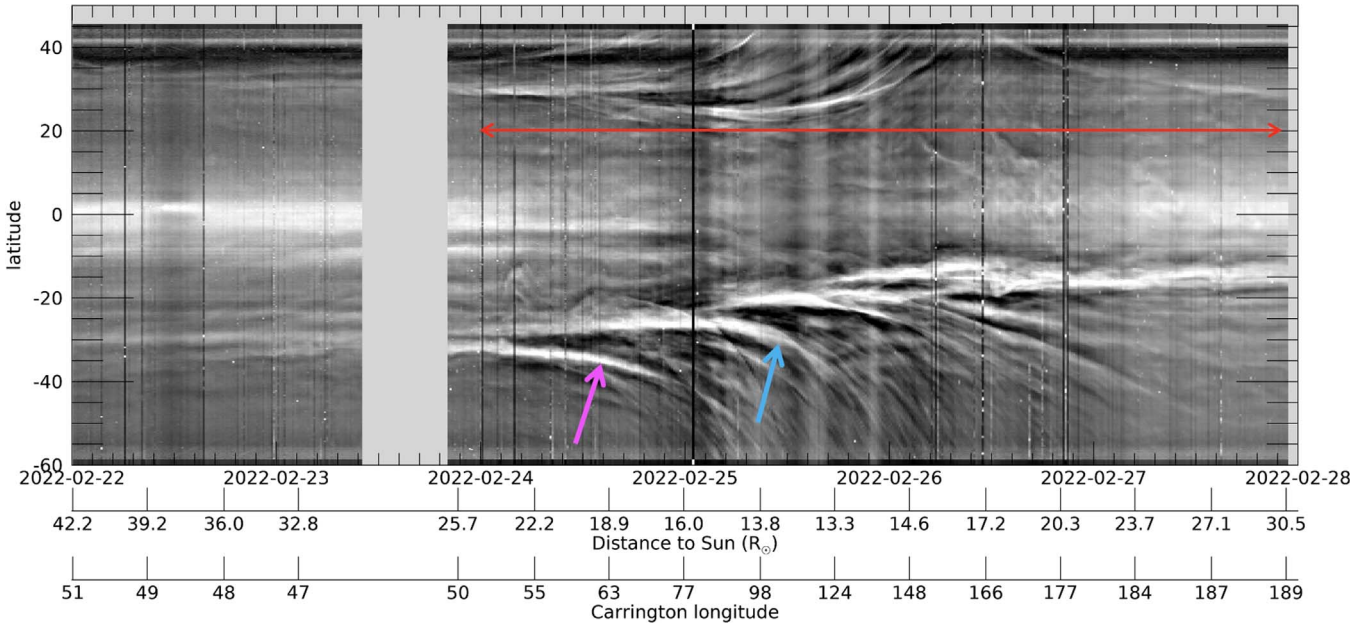


**Figure 16.** E11 lat-map made from WISPR-I L3 images for elongation range 24°–26° showing the temporal evolution in latitude at this elongation from 2022 February 22 to 28. The red arrow marks the superrotation period, when PSP was moving faster than the solar rotation rate, and PSP was flying through the coronal streamers. Multiple streamers are resolved, and large apparent changes in latitude are seen as PSP crosses the HCS on February 25. The two rays that were tracked are indicated by arrows in the colors assigned in Table 2.

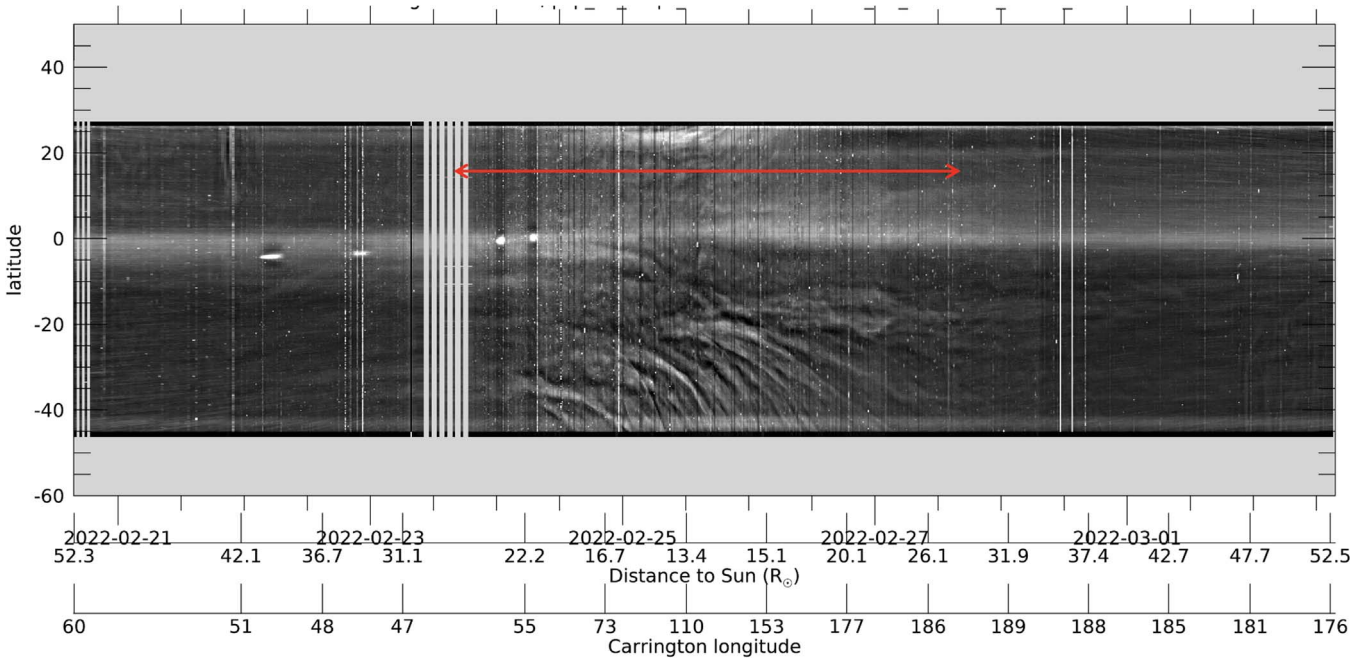


**Figure 17.** E11 lat-map from WISPR-O images for elongation range 52°–54° showing temporal evolution at this elongation from 2022 February 21 to March 2. The red arrow marks the superrotation period, when PSP was moving faster than the solar rotation rate, and PSP was flying through the coronal streamers. The effect of the improved resolution between E8 and E11 is apparent (compare with Figure 6). The diffuse white band at 0° latitude is due to Venus' dust ring (see text).

difference in the angular size of the Sun in between the images from February 24 (PSP at 19 $R_\odot$) and February 25 (PSP at 14 $R_\odot$).

### 3.3. Comparison with LASCO/C3 Observations

In this section, we compare the results of the coordinate extraction for both E11 rays with LASCO observations of the corona using a LASCO/C3 synoptic map for Carrington rotation (2254), which covers the time period that the E11 rays were tracked. Figure 19 shows the LASCO/C3 synoptic map for the west limb at a distance of 10 $R_\odot$. On top of this image, the Carrington coordinates of the rays are plotted as colored triangles, as well as the PSP orbit loop (yellow line) and HCS from the PFSS model (orange dashed line), as in Figure 14. The ray triangles are plotted in the colors assigned in Table 2 and used in other E11 figures. The ray coordinates fall on the bright band that marks the locations of the bright helmet streamers that straddle the HCS. The extracted locations are in better agreement with the LASCO/C3 bright bands than with the

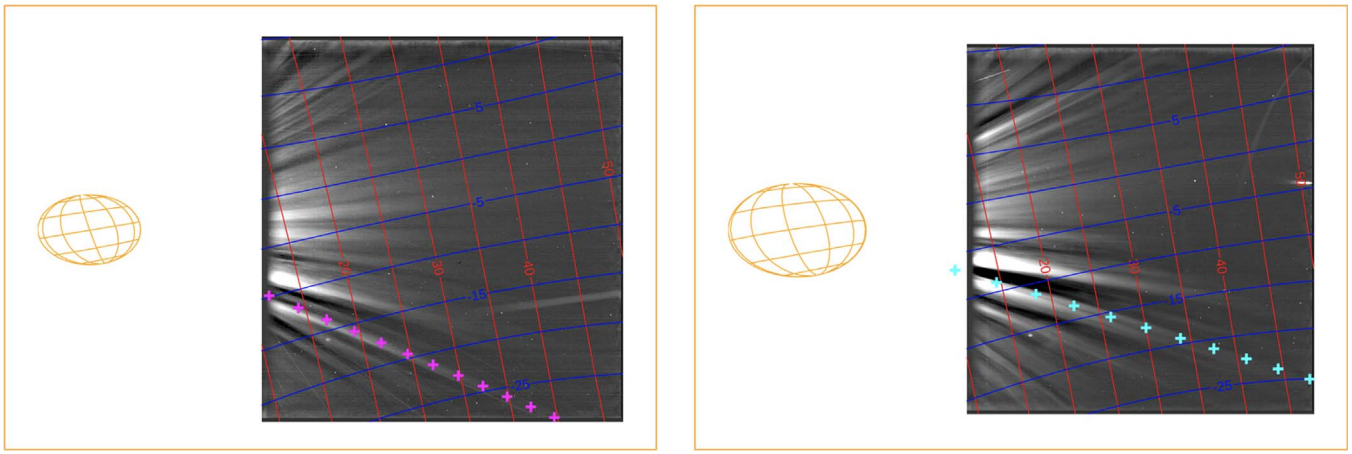

**Figure 18.** Images showing the rays whose coordinates were extracted from WISPR-I images in E11. Left: WISPR-I image for February 24 at 15 UT showing the WIS-I February 24 ray. The magenta symbols are 3D points computed from the extracted coordinates, starting at 3 $R_\odot$ in increments of 1 $R_\odot$, which have been projected back onto the image. Right: WISPR-I image for February 25 at 10 UT showing the WIS-I February 25 ray. The cyan symbols are 3D points computed from the extracted coordinates, starting at 3 $R_\odot$ in increments of 1 $R_\odot$, which have been projected back onto the image. For both rays, the points fall on the rays tracked, thus verifying the solutions.

**Table 2**
Summary of Results for Determination of Ray Coordinates for E11

| E11 Coronal Ray | WIS-I February 24 | WIS-I February 25 |
|---|---|---|
| Plotting color | magenta | cyan |
| Tracking start time | 2022-2-24T15:00 | 2022-2-25T10:00 |
| Tracking end time | 2022-2-24T22:30 | 2022-2-25T17:00 |
| **CAR frame** | | |
| Longitude (°) | $120.4 \pm 1.6$ | $164.5 \pm 0.7$ |
| Latitude (°) | $-35.6 \pm 0.7$ | $-29.7 \pm 0.2$ |
| Reduced $\chi^2$ | 1.3 | 1.6 |
| Radial extent ($R_\odot$) | 5–15 | 3–12 |
| **HCI frame** | | |
| Longitude (°) | $67.6 \pm 1.6$ | $119.7 \pm 0.6$ |
| Latitude (°) | $-38.1 \pm 0.6$ | $-31.5 \pm 0.2$ |
| Reduced $\chi^2$ | 1.7 | 2.6 |
| Radial extent($R_\odot$) | 5–16 | 3–13 |
| **Uncertainties in coordinates** | | |
| Error in longitude (°) | ±4.1 | ±2.6 |
| Error in latitude (°) | ±1.3 | ±0.9 |

**Note.** A ray's assigned color is used for identifying that ray in the various plots and figures.

HCS from the PFSS, which validates the results of our coordinate extract for these two rays. Note that the bright bands are above and below the orbit and solar equatorial plane as observed previously in the E11 lat-map in Figure 16. Presumably LASCO also viewed the HCS *face-on* on when the HCS was on LASCO's west limb around 2022 March 6, and the resulting short LOS through the HCS plasma may contribute to the void seen in the synoptic map.

## 4. Determination of Source Region of Tracked Coronal Rays

In this section, the source of the E8 and E11 tracked coronal rays is determined by mapping the extracted Carrington coordinates of the rays down into the lower corona using a PFSS magnetic field model, described below. The rays were assumed to extend radially to the source surface of the PFSS at 2.5 $R_\odot$. The rays were then mapped from the source surface to a height of 1.2 $R_\odot$ by following the field lines of the PFSS model. To test the sensitivity of the source location to the uncertainty in our coordinate extractions, two locations were also mapped from coordinates with a ±4° error added to the longitude, using the largest error in Table 1 for all rays. Thus, in the plots discussed below, the group of three mappings per ray shows the ray source and also the uncertainty in the source location resulting from the uncertainty in the extracted coordinates.

The PFSS magnetic models used are those of Schrijver & De Rosa (2003), available via SolarSoft. These models have proved to be very robust during early PSP (solar minimum) orbits (Bale et al. 2019; Panasenco et al. 2020). As a lower boundary condition, the PFSS model incorporates magnetic field maps produced by an evolving surface-flux transport model based on magnetic fields observed by the Helioseismic and Magnetic Imager (Scherrer et al. 2012; Schou et al. 2012) on the Solar Dynamics Observatory. The model evolves these fields in accordance with differential rotation, meridional flows, and convective dispersal processes. The dates for the synoptic magnetograms used for the boundary condition on the PFSS models are 2021 April 29 at 6 UT for E8 and 2022 February 25 at 12 UT for E11.

Figures 20 and 21 show the results of the magnetic mapping of the tracked rays from the source surface to 1.2 $R_\odot$ for E8 and E11, respectively. The connections are plotted on synoptic magnetograms from the PFSS for 1.2 $R_\odot$, which show contours of magnetic energy density. The neutral line at this height is the thick black line; the open field lines at this height are colored green in the north and aqua in the south. The red lines show the mapped connections from the ray coordinates at the source surface (red $x$'s) to their predicted source locations. The magnetically mapped connections (red lines) start at the ray coordinates (red $x$'s) and end at the predicted source location (the red $o$'s) at 1.2 $R_\odot$. The starting locations for the three connections per ray are enclosed in a colored oval of the ray's assigned color (Table 1 for E8; Table 2 for E11). In Figure 20, the locations for the E8 high ray that was tracked independently in WISPR-I and WISPR-O images (see Table 1) are enclosed in an oval of both colors

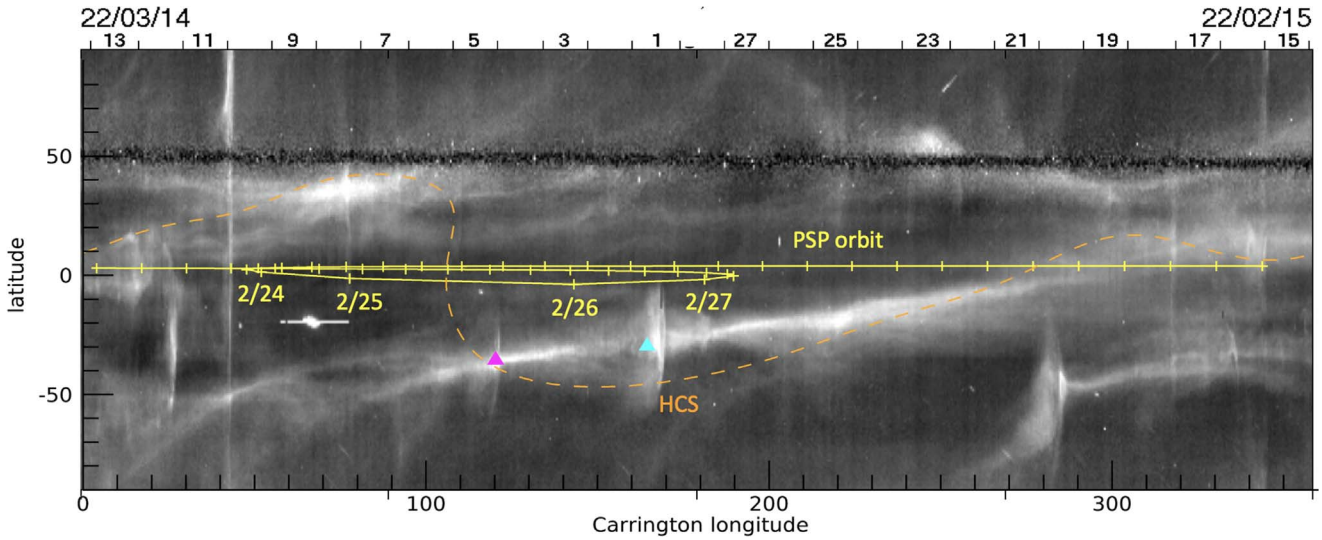


**Figure 19.** LASCO/C3 synoptic Carrington map for CR 2254 for the west limb at 10 $R_\odot$. The PSP orbit, HCS, and the extracted coordinates of the two rays are also plotted, as in Figure 3. The ray coordinates are plotted as triangles using the colors assigned in Table 2 and as used in Figure 18. Both rays fall on the bright dense bands seen in the LASCO image, confirming that these features lie in the streamer belt. See text.

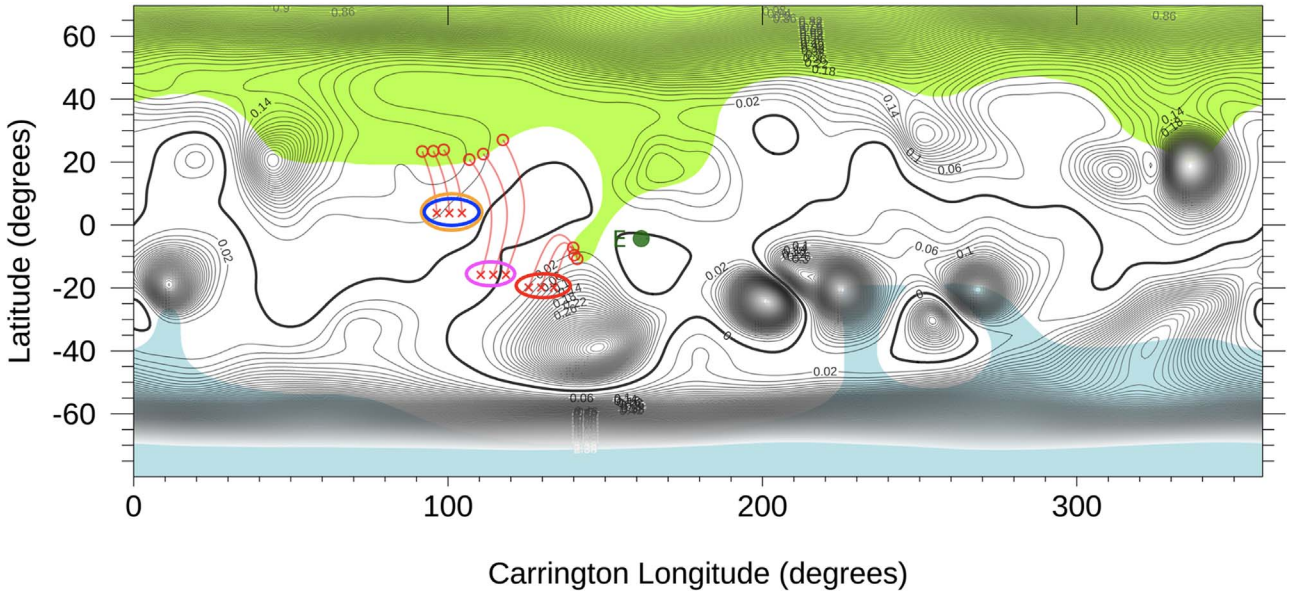


**Figure 20.** Synoptic magnetogram from the E8 PFSS magnetic model showing the magnetic mappings used to determine the source regions of the tracked coronal rays. The colored ovals enclose three $x$'s marking the Carrington coordinates (and $\pm 4°$ of longitude to account for the uncertainty) of the tracked rays. The thin red lines show the mapping from the source surface to the predicted sources (red $o$'s) at 1.2 $R_\odot$, the height of the magnetogram. The ovals enclosing the $x$'s are colored by the color assigned to the ray in Table 1; the ray at approximately 100° was tracked independently in the inner and outer telescopes, so both colored ovals are shown (orange and blue). The magnetogram shows contours of magnetic energy density at 1.2 $R_\odot$ (thin lines) and the neutral line at this height (thick black line). Open field regions at this height are shown as colored regions (lime green and aqua for north and south coronal hole regions, respectively). All sources map to the boundary of the north coronal hole.

(blue and orange). It can be seen that, for all rays, the source was traced to the boundary of a polar coronal hole or an extension. The results are insensitive to the $\pm 4°$ uncertainty in the extracted longitude. For E8 (Figure 20), the WIS-I L3 bright low ray mapped to a narrow extension of the northern coronal hole that reach down below the solar equator. The other rays all mapped to the boundary of the northern coronal hole at about 20° latitude. For E11 (Figure 21), the WIS-I February 24 ray (magenta) mapped to the southern coronal hole at about 70° south, and the WIS-O February 25 ray (cyan) mapped to an extension of the northern coronal hole reaching down below the solar equator.

## 5. Summary and Discussion

As PSP's perihelion decreases, WISPR's ability to resolve coronal structures increases dramatically, because not only is PSP closer to the Sun but also the region of sensitivity for white-light coronagraphs scales with Sun–telescope distance. Thus, WISPR is sensitive to a much more local region of the corona as it flies closer to the Sun (Vourlidas et al. 2016). Fortuitously, in encounters E8 (perihelion 15.9 $R_\odot$) and E11 (perihelion 13.3 $R_\odot$), the HCS was crossed near the perihelion where WISPR's ability to resolve structure is best. In this paper, we have shown that, as PSP flies closer to the Sun and the HCS, the streamer rays near the HCS were resolved into

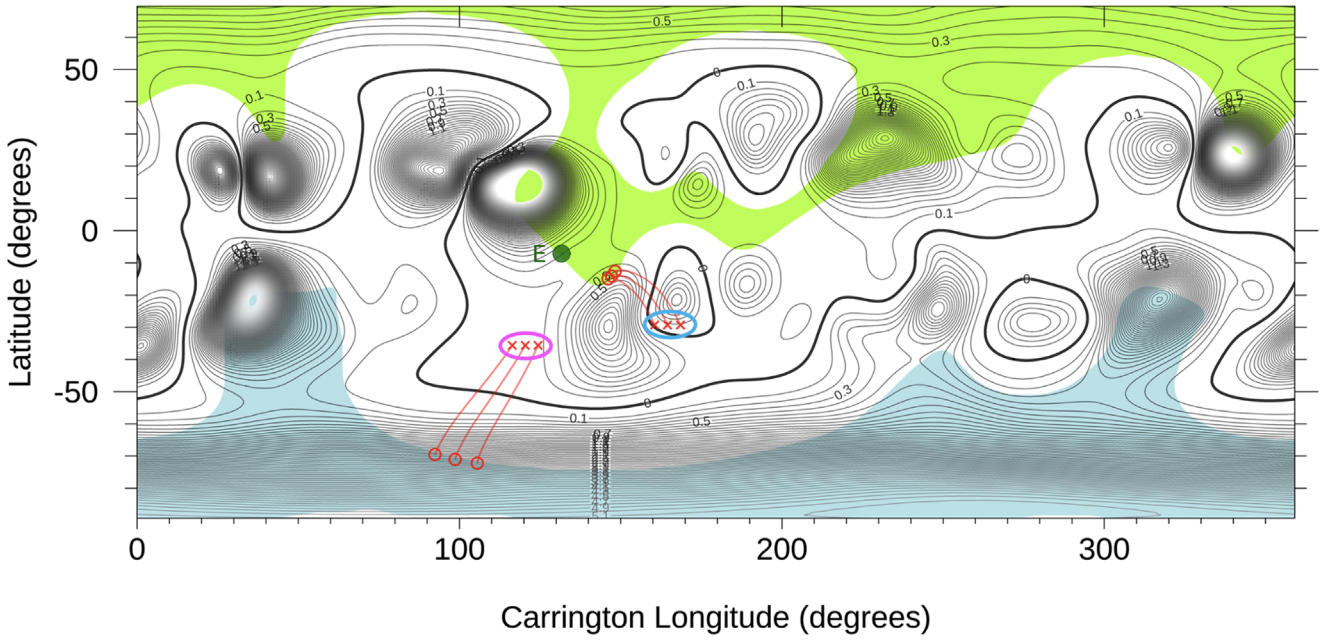


**Figure 21.** Synoptic magnetogram from the E11 PFSS model showing the mappings used to determine the source regions of the tracked corona's rays. The colored ovals enclose three x's marking the Carrington coordinates (and $\pm 4^{\circ}$ of longitude to account for the uncertainty) of the tracked rays. The thin red lines show the mapping from the source surface to the predicted sources (red *o*'s) at 1.2 $R_{\odot}$, the height of the magnetogram. The ovals enclosing the *x*'s are colored by the color assigned to the ray in Table 2. The magnetogram shows contours of magnetic energy density at 1.2 $R_{\odot}$ (thin lines) and the neutral line at this height (thick black line). Open field regions at this height are shown as colored regions (lime green and aqua for north and south coronal hole regions, respectively). Both rays map to the boundary of coronal holes, and the mappings are insensitive to the $\pm 4^{\circ}$ uncertainty in longitude.

increasingly finer-scale rays of various sizes and brightnesses, indicating that the HCS plasma sheet is composed of narrow ray-like structures, leading to large density variations in the direction transverse to the radial. The superposition of this fine-scale ray structure on the foreground and background plasma is most likely responsible for the filamentary nature of the corona seen in solar eclipse and coronagraph images (Thernisien & Howard 2006; Wang et al. 2007; DeForest et al. 2018). It may well be that the HCS itself has fine-scale wrinkles associated with the fine-scale ray structure.

Near the perihelion, PSP flies faster than the Sun rotates, and thus, PSP is literally flying through the coronal streamers as it images them. As PSP approaches the Sun, the coronal rays are resolved into fine-scale rays of varying size and brightness. Then, as PSP flies through these fine-scale rays during the superrotation period, a dramatic change (increase or decrease) in the *apparent* latitude of the rays is observed. Some rays can be seen to leave the WISPR FOV from the top or the bottom, depending on whether PSP flew under or over them. These effects were more pronounced in the E11 encounter because of WISPR's increased resolving power with decreasing distance to the Sun.

As PSP flew through the streamer belt, the multiple views of distinct rays, and specifically the rate of change of the apparent latitude, allowed us to extract their coordinates in a heliocentric frame under the assumption that the rays are stationary and radial in a heliocentric coordinate frame (Paper I). The technique involves tracking the rays in a series of images and fitting the data to analytic expressions. In the present work, we used this technique to extract the coordinates of a number of bright coronal rays in both E8 and E11. In E8, we also determined the trajectories of two transient "blobs" using a closely related tracking and fitting technique, described in Liewer et al. (2020). We have also compared their locations to an HCS from a PFSS model (Badman et al. 2020, 2022) and also to LASCO/C3 synoptic maps of the streamer belt. All eight of the features—6 rays and 2 blobs— were found to lie near the HCS and within or near the brightest band in the LASCO synoptic maps. We also used PFSS models to trace the locations of the six rays down to 1.2 $R_{\odot}$ to determine where they originate. All the rays traced to the boundaries of polar coronal holes or their extensions.

It is generally accepted that streamer blobs are the result of the weak magnetic field at the cusp of helmet streamers. Suess et al. (1996) showed that when heated, helmet streamers were not stable and could lead to opening of the flux and release of plasma into the solar wind. Motivated by LASCO observations of streamer blobs, the simulations by Rappazzo et al. (2005) and by Chen et al. (2009) showed instability of the cusp leading to the formation and recurrent release of plasma blobs from the tips of the helmet streamers. Plasmoid formation at helmet streamer tops is supported by observations (Rouillard et al. 2010; Wang & Hess 2018; Sanchez-Diaz et al. 2019). More recently, motivated by PSP in situ measurement of streamer blobs, 3D simulations were used to investigate blob formation in the context of in situ observations of streamer blobs by PSP (Réville et al. 2022). Understanding the processes involved in the formation of streamer blobs at the tips of helmet streamers remains an active area of research.

It is not yet clear what process or processes give rise to the large density variations we observed in the HCS plasma sheet. Continuous intermittent interchange reconnection between open and adjacent closed magnetic field lines, whether in active or quiet Sun regions, is generally accepted to play a major role in creating streamer belt wind, because, in this process, plasma from the closed loop is transferred to the open loop. This process can explain not only why the streamer belt wind is so variable but also why its composition is like that of

coronal plasma in heated, closed loops versus that of fast wind from coronal holes (Zurbuchen et al. 2000). Wang et al. (2007) attributed all three types of coronal streamers—helmet streamers, pseudostreamers, and polar plumes—to magnetic reconnection between closed coronal loops and adjacent open field lines. By comparing solar eclipse and LASCO images with PFSS models, they found that all visible rays were "in fact rooted inside or along the boundaries of coronal holes."

Building on the interchange concept of the slow wind resulting from reconnection along the open–closed field boundary, Antiochos et al. (2011) introduced the concept of the Separatrix-Web (S-Web) to explain the large angular width of the slow solar wind band. The S-Web, a network of magnetic separatrices in the corona magnetic field, creates a web of open-field corridors. Continuous interchange reconnection along this web, then, could create the slow solar wind. 3D MHD calculations showed that this web extended far enough from the HCS to explain the observed width of the slow wind band. Both flux emergence and photospheric footpoint motion were invoked as drivers of the interchange reconnection. Higginson et al. (2017), using 3D MHD simulations with a simplified model corona, found that interchange reconnection along the S-Web boundary could be driven by photospheric footpoint motions at the supergranule scale.

Analysis of extreme ultraviolet (EUV) observations of the evolution of coronal hole boundaries by Madjarska & Wiegelmann (2009) showed that, while the general shape of coronal holes evolves slowly, the boundaries are very dynamic on short spatial and temporal scales. Small loops associated with coronal bright points were observed to play an essential role in the dynamics, with their frequent emergence and disappearance continuously expanding or contracting the coronal hole boundaries. In a subsequent paper, the association of bright points with small-scale changes at coronal hole boundaries was confirmed using Hinode X-ray observations of coronal bright points (Subramanian et al. 2010). In addition, frequent plasma outflows were observed to originate from preexisting or emerging X-ray bright points near the coronal hole boundaries. Subramanian et al. (2010) concluded that the ejections were triggered by interchange reconnection between the closed magnetic field lines of the bright points and the open field lines of the coronal hole, and suggested that the outflows might be a source of slow solar wind.

Based on EUV solar observations and very high-resolution magnetograms from the Big Bear Solar Observatory, Raouafi et al. (2023) have recently proposed that the EUV bright points may be the sites of interchange reconnection that are the primary source of the energy that heats and drives the solar wind. Each interchange event produces a short-lived plasma jet of hot plasma and Alfvén waves; a calculation of the frequency and energy of such events suggests they can supply the energy needed (Raouafi et al. 2023). Earlier, under the assumption that magnetograms from the Heliospheric Magnetic Imager (HMI) had greatly underestimated the amount of minority-polarity flux inside unipolar regions, Wang (2020) calculated that the interchange reconnection associated with minority polar inclusions could supply the necessary energy to heat the corona and drive the solar wind. He based the underestimation assumption on a detailed analysis of EUV images from the Atmospheric Imaging Assembly (AIA) and corresponding HMI magnetograms; evidence of reconnection was seen in AIA images where no minority inclusions were seen in the magnetograms. The energy released in the reconnection events will be in the form of ohmic heating, jets, and MHD waves; the heating can also lead to a mass flux via chromospheric evaporation (Wang 2020). In his "hybrid" solar wind model, interchange reconnection heats the lower corona and drives the mass flux, whereas waves impart energy and momentum to the outflowing wind at greater distances. The final speed of the wind will depend on the expansion of the flux tube (Wang 2020).

Interchange reconnection associated with minority-polarity flux emergence and coronal bright points near polar CH boundaries could lead to the large density variations in HCS plasma sheet observed by WISPR, reported in here. The observations cited above (Madjarska & Wiegelmann 2009; Subramanian et al. 2010) show that the bright points are also associated with the small-scale, continuous reconfiguration of coronal hole boundaries and, thus, could lead to the variations in the plasma density of the HCS, as reported here. Another possible explanation is the interchange reconnection between the closed loops associated with active regions that are near the open field lines of the helmet streamers. Both may contribute since we see rays of varying degrees of brightness. When PSP reaches a perihelion of $11.6\,R_{\odot}$ in 2023, WISPR's resolving power will increase even further, and the inner edge of the field of view will reach into $2.7\,R_{\odot}$. This, coupled to unique new observations from Solar Orbiter and the Daniel K. Inouye Solar Telescope, may further clarify the processes leading to the variability in the coronal streamers and their relation to the slow solar wind.

We are grateful to Prof. Marco Velli for many helpful discussions about the corona and reconnection. We thank S. Badman for supplying the HCS data from his PFSS models for both E8 and E11 and thank the SWEAP team for the use of their data. We thank P. Hess, B. Gallagher, and the entire WISPR team for their support. Parker Solar Probe was designed, built, and is now operated by the Johns Hopkins Applied Physics Laboratory as part of NASA's Living with a Star (LWS) program (contract NNN06AA01C). Support from the LWS management and technical team has played a critical role in the success of the Parker Solar Probe mission. The Wide-Field Imager for Parker Solar Probe (WISPR) instrument was designed, built, and is now operated by the US Naval Research Laboratory in collaboration with Johns Hopkins University/Applied Physics Laboratory (JHU/APL), California Institute of Technology/Jet Propulsion Laboratory, University of Goettingen, Germany, Centre Spatiale de Liege, Belgium, and University of Toulouse/Research Institute in Astrophysics and Planetology. The work of P.C.L. and P.P. was conducted at the Jet Propulsion Laboratory, California Institute of Technology under a contract from NASA. A.V., G. S., and R.H. are supported by the WISPR phase (E) program at JHU/APL. J.Q. is partly supported by NASA's Heliophysics Guest Investigator program (80NSSC22K0519). C.B. is supported by the NASA STEREO/SECCHI (NNG17PP27I) program.

## Appendix

Several light sources contribute to the signal in WISPR calibrated images (Hess et al. 2021). Namely, the K-corona emission (photospheric light Thomson-scattered by the free

electrons) along with the zodiacal light (photospheric light scattered by dust in the interplanetary medium, also referred to as the F-corona), diffuse galactic sources, nonresolved starlight, and stars and planetary objects. In order to reveal the fainter K-corona, the zodiacal light must be removed. This is more challenging for WISPR compared to white light imagers at 1 au (Stenborg et al. 2022).

Two such algorithms, which can reveal discrete features in both the K-corona (e.g., coronal transients and streamers) and F-corona (dust rings, asteroid and cometary trails), were described in the Appendix of Howard et al. (2022). Here, we describe a third algorithm, which is used routinely to generate the L3 WISPR data products, which were used for most of the analysis in this work. These products are available at https://wispr.nrl.navy.mil/wisprdata.

The idea behind this algorithm is similar to that used for the "LT" data product, described in Appendix B of Howard et al. (2022). The procedure is totally heuristic and can be tuned by varying the free parameters of the algorithm—the results depend upon the spatial scales of the discrete features of interest. Briefly, a proxy background, $B$, for each calibrated image, $I$, is created first through a series of straightforward steps:

1. the reduction of the contaminating effect of bright point-like sources, such as planets or stars, by applying a σ filter to each WISPR image (as implemented in the IDL SolarSoft with the "sigma_filter.pro" routine),
2. the noise reduction of the brightness profile $I_j$ at each WISPR image column $j$ ($j = 0 \ldots 959$) by applying a running median filter with a window of size $k$ pixels (hereafter $I_j^m$),
3. smoothing $I_j^m$ by applying a boxcar running average with a window of size $h$ pixels (hereafter $I_j^{ms}$),
4. detrending of $I_j$ by normalizing $I_j$ with $I_j^{ms}$, i.e., $I_j^N = I_j / I^m s_j$,
5. the determination of the running fifth percentile of $I_j^N$ with a window size of "$g$" pixels (hereafter $I_{5_j}^N$),
6. further noise reduction and smoothing by applying steps (2) and (3) on $I_{5_j}^N$ (hereafter $I_{5ms_j}^N$),
7. the determination of the ground level by computing the median of $I_{5ms_j}^N$ (hereafter $b_0$),
8. the determination of the base brightness level of $I_j$ as $B_j = I^m s_j{}^* b_0$.

The values of the free parameters ($k$, $h$, and $g$) are chosen by the user. In its actual implementation, for $960 \times 1024$ pixels$^2$ images, the values are as follows: $k = 61$, $h = 71$, $g = 61$. Once the proxy background for each image is obtained, we remove it by taking either the ratio or the difference. The former has the advantage that it removes the radial dependence of the K-corona, and hence allows for the visualization of the K-corona structures farther out. On the other hand, the latter preserves the physical units of the calibrated images at the expense of keeping a strong radial intensity gradient in the resulting difference images.

Either approach (*ratio* or *difference*) enhances the instrumental artifacts. A grand minimum model, $G$, must then be created to account for them. Since the variable F-corona (due to the rapidly changing position of the observer) is no longer present, the standard exploitation of the time domain can be used as in the case for white light images at 1 au. The simplest way to create $G$ is to stack the background removed images and take the median in time. The time window of each encounter is about 10 days, during which the spacecraft travels more than 200° in longitude. Although this ensures that the K-corona structures are not static in the FOV, remnant coronal rays can be seen in $G$ if images from only a single encounter are considered. Therefore, to create $G$, it is best to use as many encounters with the same orbital geometry as possible to minimize the presence of remnant coronal structures in the grand minimum model.

Another caveat is that creating the background model is not straightforward in the case of the *difference* approach because of the higher K-corona brightness level, and changing gradient as the observer approaches the Sun (e.g., the inner edge of WISPR FOV reaches as close as $3.1\,R_\odot$ at encounter (11) perihelion). In this case, the overall brightness of each background difference image must be first normalized to a fixed distance to create the grand minimum model. This is done by multiplying each difference image, $D_i = I_i - B_i$, by a factor $f_i = (r_0/r_i)^n$ where $r_0 = 0.2$ au is the arbitrary observer's reference heliocentric distance and $r_i$ is the observer's distance at the time of each image. Then, to create the grand minimum model, $G$, we compute the time median of the data cube formed by the normalized difference images. The value of $n$ is determined heuristically, such that the time evolution of the median value of the normalized $D_i$ shows the minimum trend with the observer's distance (we found $n = 2.3$).

The resulting L3 difference images, $L_i$, are computed as $L_i = (D_i^* f_i) - G + \mathrm{median}(G)$.

We note that the creation of the grand minimum model became more challenging starting with E10 because of the closer approach of the S/C to the Sun, which translated in a steeper change of the K-corona brightness near the perihelion. Therefore, the grand minimum model correction has not been applied for E10 onward. This explains why the Venus dust ring is seen in E11 maps, but not in E8. Namely, the excess brightness band from the dust ring is a stationary feature and hence is present in the grand minimum background model.

## ORCID iDs

Paulett C. Liewer https://orcid.org/0000-0002-5068-4637
Angelos Vourlidas https://orcid.org/0000-0002-8164-5948
Guillermo Stenborg https://orcid.org/0000-0001-8480-947X
Russell A. Howard https://orcid.org/0000-0001-9027-8249
Jiong Qiu https://orcid.org/0000-0002-2797-744X
Olga Panasenco https://orcid.org/0000-0002-4440-7166
Carlos R. Braga https://orcid.org/0000-0003-1485-9564

## References

Antiochos, S. K., Mikić, Z., Titov, V. S., Lionello, R., & Linker, J. A. 2011, ApJ, 731, 112
Arge, C. N., Henney, C. J., Koller, J., et al. 2010, in AIP Conf. Ser. 1216, Twelfth International Solar Wind Conf., ed. M. Maksimovic (Melville, NY: AIP), 343
Badman, S. T., Bale, S. D., Martínez Oliveros, J. C., et al. 2020, ApJS, 246, 23
Badman, S. T., Brooks, D. H., Poirier, N., et al. 2022, ApJ, 932, 135
Bale, S. D., Badman, S. T., Bonnell, J. W., et al. 2019, Natur, 576, 237
Bale, S. D., Goetz, K., Harvey, P. R., et al. 2016, SSRv, 204, 49
Brueckner, G. E., Howard, R. A., Koomen, M. J., et al. 1995, SoPh, 162, 357
Chen, Y., Li, X., Song, H. Q., et al. 2009, ApJ, 691, 1936
DeForest, C. E., Howard, R. A., Velli, M., Viall, N., & Vourlidas, A. 2018, ApJ, 862, 18
Decraemer, B., Zhukov, A. N., & Van Doorsselaere, T. 2019, ApJ, 883, 152

Fox, N. J., Velli, M. C., Bale, S. D., et al. 2016, SSRv, 204, 7
Hess, P., Howard, R. A., Stenborg, G., et al. 2021, SoPh, 296, 94
Higginson, A. K., Antiochos, S. K., DeVore, C. R., Wyper, P. F., & Zurbuchen, T. H. 2017, ApJ, 837, 113
Howard, R. A., Moses, J. D., Vourlidas, A., et al. 2008, SSRv, 136, 67
Howard, R. A., Stenborg, G., Vourlidas, A., et al. 2022, ApJ, 936, 43
Howard, R. A., Vourlidas, A., Bothmer, V., et al. 2019, Natur, 576, 232
Kasper, J. C., Abiad, R., Austin, G., et al. 2016, SSRv, 204, 131
Liewer, P., Vourlidas, A., Thernisien, A., et al. 2019, SoPh, 294, 93
Liewer, P. C., Qiu, J., Ark, F., et al. 2022, SoPh, 297, 128
Liewer, P. C., Qiu, J., Penteado, P., et al. 2020, SoPh, 295, 140
Madjarska, M. S., & Wiegelmann, T. 2009, A&A, 503, 991
Nindos, A., Patsourakos, S., Vourlidas, A., et al. 2021, A&A, 650, A30
Panasenco, O., Velli, M., D'Amicis, R., et al. 2020, ApJS, 246, 54
Poirier, N., Kouloumvakos, A., Rouillard, A. P., et al. 2020, ApJS, 246, 60
Raouafi, N. E., Stenborg, G., Seaton, D. B., et al. 2023, ApJ, 945, 28
Rappazzo, A. F., Velli, M., Einaudi, G., & Dahlburg, R. B. 2005, ApJ, 633, 474
Réville, V., Fargette, N., Rouillard, A. P., et al. 2022, A&A, 659, A110
Rouillard, A. P., Davies, J. A., Lavraud, B., et al. 2010, JGRA, 115, A04103
Sanchez-Diaz, E., Rouillard, A. P., Lavraud, B., Kilpua, E., & Davies, J. A. 2019, ApJ, 882, 51
Scherrer, P. H., Schou, J., Bush, R. I., et al. 2012, SoPh, 275, 207
Schou, J., Scherrer, P. H., Bush, R. I., et al. 2012, SoPh, 275, 229
Schrijver, C. J., & De Rosa, M. L. 2003, SoPh, 212, 165
Sheeley, N. R. J., Lee, D. D. H., Casto, K. P., Wang, Y. M., & Rich, N. B. 2009, ApJ, 694, 1471
Stansby, D., Yeates, A., & Badman, S. 2020, JOSS, 5, 2732
Stenborg, G., Howard, R. A., Vourlidas, A., & Gallagher, B. 2022, ApJ, 932, 75
Subramanian, S., Madjarska, M. S., & Doyle, J. G. 2010, A&A, 516, A50
Suess, S. T., Wang, A. H., & Wu, S. T. 1996, JGR, 101, 19957
Thernisien, A. F., & Howard, R. A. 2006, ApJ, 642, 523
Vourlidas, A., & Howard, R. A. 2006, ApJ, 642, 1216
Vourlidas, A., Howard, R. A., Plunkett, S. P., et al. 2016, SSRv, 204, 83
Wang, Y. M. 2020, ApJ, 904, 199
Wang, Y. M., Biersteker, J. B., Sheeley, N. R. J, et al. 2007, ApJ, 660, 882
Wang, Y. M., & Hess, P. 2018, ApJ, 859, 135
Wang, Y. M., Sheeley, N. R., Socker, D. G., Howard, R. A., & Rich, N. B. 2000b, JGR, 105, 25133
Wang, Y. M., Sheeley, N. R. J., Howard, R. A., et al. 1997, ApJ, 485, 875
Wang, Y. M., Sheeley, N. R. J., & Rich, N. B. 2000a, GeoRL, 27, 149
Wang, Y. M., Sheeley, N. R. J., Walters, J. H., et al. 1998, ApJL, 498, L165
Zurbuchen, T. H., Hefti, S., Fisk, L. A., Gloeckler, G., & Schwadron, N. A. 2000, JGR, 105, 18327